Astron. Astrophys. 309, 581–611 (1996)

ASTRONOMY AND ASTROPHYSICS

The structure of the IC 1396 region*

Helmut Weikard [1,2], Jan G.A. Wouterloot [2], Alain Castets [1], Gisbert Winnewisser [2], and Koji Sugitani [3]

[1] Groupe d'Astrophysique, Observatoire de Grenoble, B.P. 53 X, F-38041 Grenoble CEDEX, France
[2] I. Physikalisches Institut, Universität zu Köln, Zülpicher Straße 77, D-50937 Köln, Germany
[3] College of General Education, Nagoya City University, Mizuho-ku, Nagoya 467, Japan

Received 10 March 1995 / Accepted 18 August 1995

Abstract. We have made an extensive study of the molecular clouds associated with the H II region IC 1396 in the rotational transitions J=1−0 and J=2−1 of ^{12}CO and ^{13}CO and J=3−2 of ^{12}CO with an average spatial resolution of 2.′5 and an average sampling of about 2.′0, in order to get information on its structure and evolution.

On the basis of our observations, which cover an area of more than 6 deg^2, we can classify the molecular clouds into those directly associated with the ionizing O6.5V star HD 206267, producing the bright-rimmed clouds, and the cold gas along the line of sight, which is mainly foreground material. The bright-rimmed clouds show the presence of warmer molecular gas through higher ^{12}CO (2−1)/(1−0), ^{13}CO (2−1)/(1−0) and ^{12}CO (3−2)/(2−1) line ratios than the cold foreground gas. The warm clouds form roughly a shell-like arrangement with a diameter of 25 to 40 pc around HD 206267 (though most are slightly closer to the Sun than the O star), and they seem to be the remainder of the now dispersing molecular cloud which gave birth to the O6.5 star and the star cluster Tr 37 associated with it. All bright-rimmed clouds show internal structure on all size scales, including bipolar outflows. Optical, FIR (IRAS 12 to 100 μm) and CO maps are in close agreement over the whole region, especially for the bright-rimmed clouds: Exceptions are some optically bright (ionized) regions, which show FIR, but no CO emission, and the cold foreground clouds, which are very weak at FIR wavelengths.

The entire mass of the mapped IC 1396 region is estimated to be 12 000 $M_\odot$, which is composed of molecular (4000 $M_\odot$), atomic (5000 $M_\odot$), and ionized material (3000 $M_\odot$) in nearly equal amounts. The masses of the bright-rimmed clouds range from a few to several 100 $M_\odot$.

Key words: interstellar medium: molecular clouds, H II regions, individual objects: IC 1396, kinematics and dynamics – ISM: molecules – radio lines: ISM

1. Introduction

The shell-like H II region IC 1396 (catalogued by Sharpless (1959) as S 131), situated in Cepheus in the local (Orion) arm, exhibits a most remarkable system of bright-rimmed clouds (see Fig. 1). IC 1396 is mainly excited by the O6.5V star HD 206267 (Crampton & Redman 1975, Walborn & Panek 1984), which is a trapezium system (Abt 1986) located almost in the centre of the H II region. HD 206267 is the brightest member of the young (about 5 Myr, Marschall et al. 1990) open cluster Tr 37 (Trumpler 1930), which contains in addition some 20 B stars, and which forms the southern nucleus of the Cep OB 2 association (Simonson 1968). Possibly related to the cluster is an X-ray pulsar (Koyama et al. 1991) located about 25′ south of HD 206267.

HD 206267 ionizes the surface layers of at least 10 small bright-rimmed molecular clouds, which are morphologically quite different. The geometry of this system is almost face-on, the clouds are relatively small and isolated, and there is little confusing fore- or background material. Compared to e.g. Orion A, NGC 2244, IC 1805 and IC 1848, which are ionized by clusters of O stars and associated with much more massive molecular clouds, IC 1396 is less complex, and excitation conditions should be better defined.

Therefore, the bright-rimmed molecular clouds facing HD 206267 provide an ideal testing ground for the investigation by means of a multi-line CO study of the effects of photon dominated regions (PDRs; formerly called photon dissociation regions) on the clouds and their connection to star formation.

The published data are rather incomplete (cf. Heske & Wendker 1985, Gyulbudaghyan et al. 1986) or show poor spatial resolution (Leisawitz et al. 1989). Some molecular work has been done on the rims A and E (cf. Loren et al. 1975, Wootten et al. 1983). Nakano et al. (1989) and Serabyn et al. (1993) report on high-resolution observations of these rims. Recently, Patel et al. (1995) made an extensive map of the region in ^{12}CO and ^{13}CO (1→0) with the FCRAO 14 m telescope.

The aim of the present project is twofold. First, the complete survey at modest single-dish resolution (3′) of the whole region (about 6 deg^2) in ^{12}CO and ^{13}CO (1→0) and also in neutral

* The complete Tables 2 to 5 are only available in electronic form at CDS via ftp 130.79.128.5

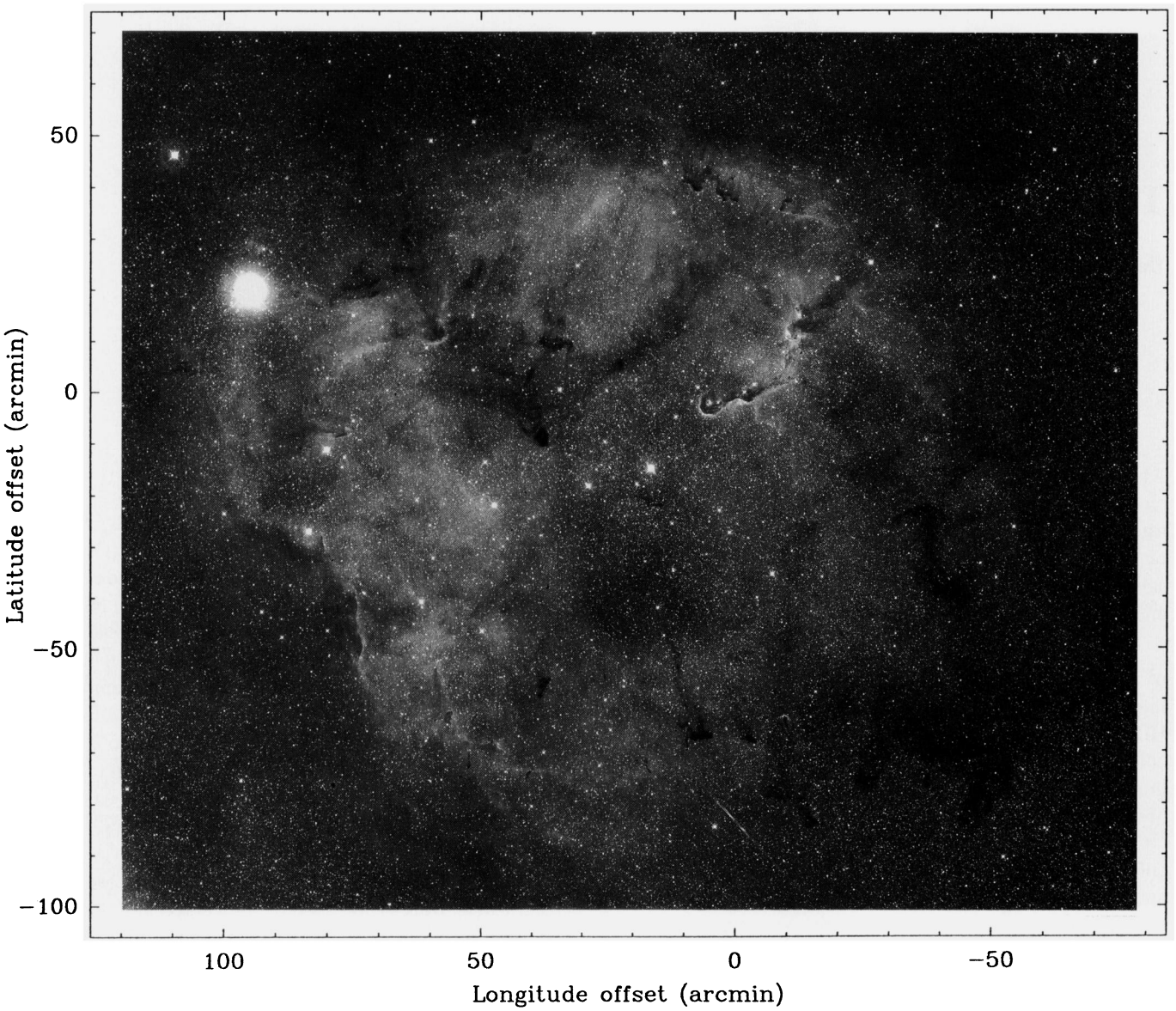

Fig. 1. Reproduction of an optical photograph of IC 1396 (by courtesy of K. Birkle, MPIA Heidelberg). The original red plate (610–690 nm) had been exposed 75 min on August 17, 1984 at the 80/120 cm Schmidt telescope on Calar Alto, Spain. Here and in all following maps the (0,0) position corresponds to (l,b) = (99.0,+4.0).

hydrogen is an indispensable step to get information on the history and structure of the entire system and on average physical parameters (masses, densities and temperatures) of the individual molecular clouds. Second, from the multi-line study of the bright-rimmed clouds using in addition the (2→1) and (3→2) transitions (and in rim A at one position C I at 492 GHz), we can investigate the excitation conditions within the clouds associated with HD 206267. Besides, we can compare the IRAS maps with our CO maps, and IRAS properties of the bright-rimmed clouds should give more insight into the morphology of the region.

In Sect. 2 we give an overview of the characteristics of the IC 1396 region and its environment. In Sect. 3 we present details on the CO and H I observations and on IRAS data. The results of our survey concerning the global view on the region and the constituent parts are displayed in Sect. 4, and our IRAS results are shown in Sect. 5. Sect. 6 is devoted to a more detailed discussion of the individual clouds, and in Sect. 7 we analyse our results. A preliminary account of some aspects of this work has been reported by Weikard et al. (1991).

2. Morphology of IC 1396

The Cep OB 2 association at a mean distance of 800 pc (Georgelin & Georgelin 1976) is part of the local feature of the galactic spiral structure and comprises the open clusters NGC 7160 [centred at (l,b)=(104.0,+6.45)] and Tr 37 [at (99.3,+3.7)], whose ages are estimated to be around 10 and

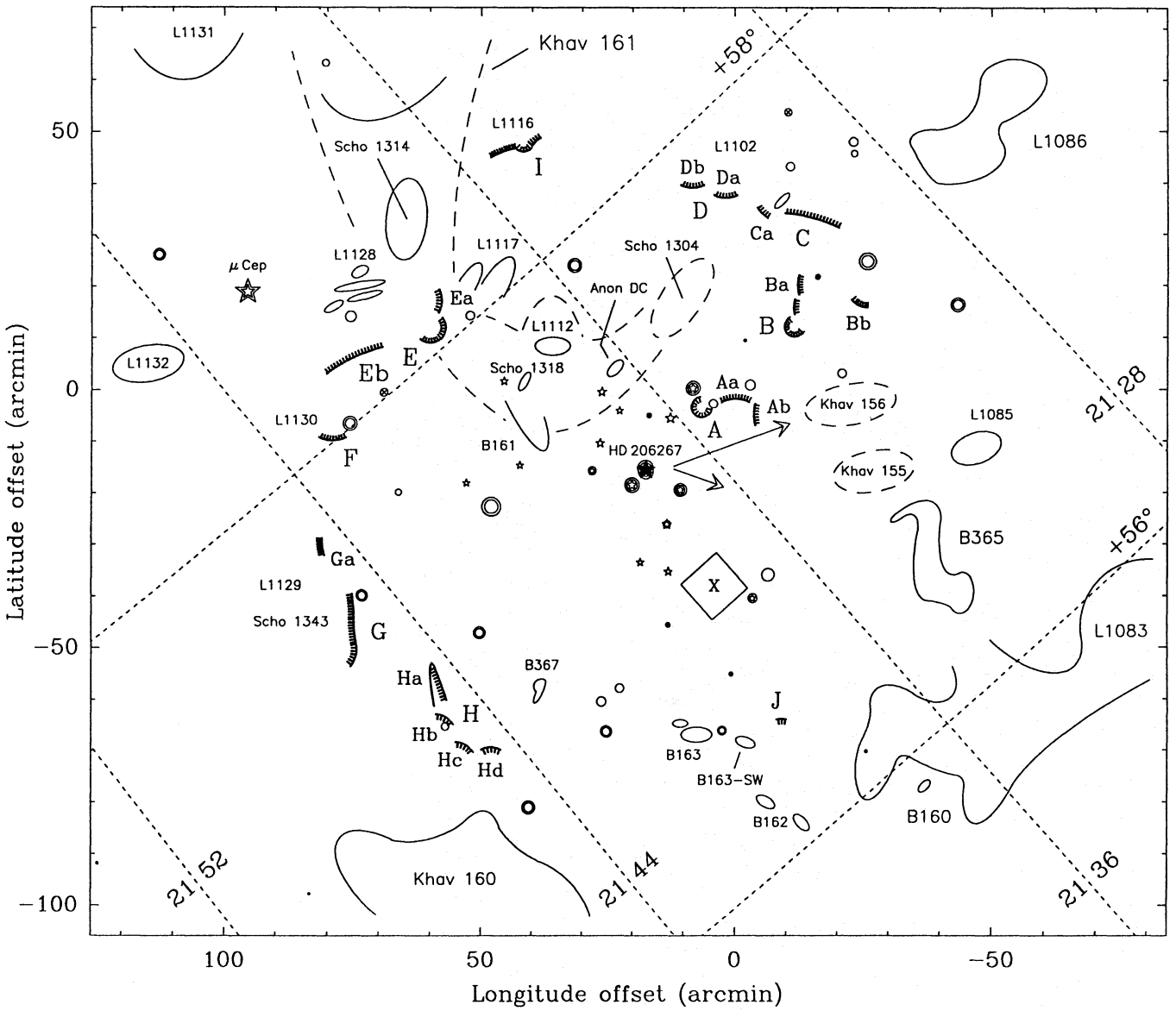

Fig. 2. Schematic finding chart for named objects in the line of sight towards IC 1396. The bright rims are hatched and named A to H following Pottasch (1956), but have been complemented by rims I and J and the subdivision of various rims, indicated by double lettering. The names of associated dark clouds or globules are included with the exception of L1105 (rim A), L1099 (rim Ab), Scho 1288 (rim B) and L1121 (rim E). Other dark and diffuse clouds are sketched by solid and dashed lines, respectively. The 17 brightest members of the open cluster Tr 37 (cf. Marschall and van Altena 1987) are indicated by star symbols. B stars of earlier type than B3, later-type B stars and B stars with unknown spectral subtype are marked by two concentric, single and crossed circles, respectively. The proper motions of HD 206267 and of the cluster are indicated by the longer and shorter arrow, respectively (for more details see Sect. 7). The position error box of the X-ray pulsar is given as well (cf. Koyama et al. 1991). Here and in all following maps, HD 206267 and the M2 supergiant μ Cep are shown for reference as a filled star symbol at (17, −16) and as a large star symbol at (96, 19), respectively.

5 Myr, respectively (Simonson 1968, Battinelli & Capuzzo-Dolcetta 1991).

The older subgroup NGC 7160 in the north is located about 2°east of the approximate centre [at (l,b)=(103.0,+8.0)] of a giant bubble (diameter of about 8°, or 110 pc) visible in IRAS brightness maps at 60 and 100 μm (Kun et al. 1987). NGC 7160 is not closely associated with H I (Simonson & van Someren Greve 1976), nor with far-infrared emission (Kun et al. 1987), nor with molecular clouds (Dobashi et al. 1994). These probably have been completely dispersed within the last 5 to 10 Myr.

Concerning the presence of atomic gas, dust and molecular clouds, the situation is quite different for the younger subgroup of Cep OB 2 in the south, Tr 37, which is associated with the H II region IC 1396. The appearance of this interstellar gas is dominated by a high degree of fragmentation into a large number

of dark and bright-rimmed globules (Fig. 1), all witness of an eventful past.

The distance towards IC 1396 is not well-determined: Simonson (1968) reported 1100 pc, Garibdzhanyan (1984) 660 pc, and Abt (1986) assumed 900 pc as distance to HD 206267. We adopt 750 pc (Becker & Fenkart 1971, Battinelli & Capuzzo-Dolcetta 1991). The H II region IC 1396 covers about 6 deg^2 in the sky, which then corresponds to a linear diameter of 36 pc.

IC 1396 is an evolved H II region, and there are probably no compact H II regions in this area. Continuum maps of IC 1396 at 2695 MHz with a spatial resolution of 4.′7 show a remarkable agreement with the large-scale optical emission, which implies a fairly uniform foreground extinction of about $A_V = 1^m.2$ (Matthews et al. 1980, Wendker & Baars 1980). HD 206267 is capable of ionizing IC 1396 without need for contributions of other stars.

The optical photograph (taken by K. Birkle using the Schmidt telescope on Calar Alto) shown in Fig. 1 reveals a diffuse H II region surrounding the exciting O6.5V star HD 206267. The northern part of the ring (or shell) is much brighter than the southern part, giving the impression of a horseshoe-type structure (cf. Wendker & Baars 1980, Heske & Wendker 1985) with its open side facing south. A minimum in brightness can be seen about 25′ southeast of HD 206267.

For easier comparison of the optical photograph (Fig. 1) with our observational (CO and FIR) data in Figs. 2 to 5, 11, and 12, we present all these figures on the same scale, and Figs. 6 and 10 show the same area. North is approximately (deviation about 3°) to the upper left and east to the lower left corner (cf. Fig. 2). The two visually brightest stars, HD 206267 at (17,−16) and the M2 supergiant μ Cep at (96,19), appear as reference points in all maps.

Fig. 1 shows, apart from the emission nebula, a multitude of conspicuous polymorphic bright-rimmed dark clouds which are clearly associated with HD 206267 due to the fact that the rims always appear at the cloud's side facing the exciting star (see Fig. 1 and Pottasch 1956).

The locations of the bright rims are sketched in a pathfinder map (Fig. 2) and labeled (counterclockwise with respect to HD 206267) as rim A through rim H (following Pottasch 1956). We designate as Aa, Ab, Ba, etc., I and J some additional bright-rimmed features:

The rim Aa cloud, 7′ southwest of rim A, seems to be physically connected with the main globule. The rims Ab and Bb are located about 10′ southwest of rims A and B, respectively, Ba 8′ northwest of rim B. Rim E is elongated northwestward and northeastward by about 10′ and 20′, respectively, and we shall refer to these parts as rim Ea and rim Eb. Rim I is rather faint, associated with L1116, and located in the very north of the H II region. Rim J, a tiny cloudlet in front of HD 206267, thus illuminated from behind and not very conspicuous on the optical photograph, was first studied by Duvert et al. (1990).

The visual appearance of the bright-rimmed clouds differs significantly: Some rims (A, Aa, Ba, E, F, G, and I) seem to be more homogeneous, other rims (B, C and D) show complex structures on a scale less than 1′ on the optical photograph. Especially rim H is made up of at least four smaller bright-rimmed cloud structures, possibly indicating fragmentation under the influence of the ionizing radiation from HD 206267. Also the brightness of the objects is different: The clouds Ba, Eb and Ab are brighter, i.e. probably illuminated at the frontside, whereas the clouds H, G, F, B, E, D, A, and Aa get darker, roughly in this order, obviously indicating an illumination from the side or from behind.

It is not clear from Fig. 1 if certain bright-rimmed clouds, e.g. those belonging to rims D, G, and I, are more extended beyond the outer perimeter of the H II region or not.

Copies from POSS prints (enlarged by a factor of about 4.5 with respect to Fig. 1) can be found for a number of the bright rims in the catalogue of Sugitani et al. (1991) (entries 32 to 42 in their Fig. 1).

Fig. 2 also shows the positions of cluster members of Tr 37 (Marschall & van Altena 1987). They are all located in the centre of IC 1396 and surrounded by the rims. There is also ongoing low-mass star formation in IC 1396: Studies of IRAS point sources (Kun & Pásztor 1990, Schwartz et al. 1991) revealed a number of young stellar object candidates with relatively low luminosity. Two outflows, an unmistakable sign of star formation, have been detected in bright-rimmed globules associated with the H II region (Sugitani et al. 1989, Duvert et al. 1990). The latter work on rim J shows that even the smallest clumps so far observed show bipolar outflow activity, possibly indicating a high star-forming efficiency induced by ionization shock fronts (cf. Klein et al. 1985) stemming from HD 206267.

As conspicuous as the bright rims are in Fig. 1 a number of highly irregularly shaped dark patches (globules) which display sharp contoured edges against the illuminated background, but which do not show bright rims. The bright-rimmed and other (normal) dark clouds and globules have been catalogued by Barnard (1927), Khavtassi (1960), Lynds (1962) [for revised positions of globules see Parker (1988)] or Schoenberg (1964), and we have sketched their outlines in Fig. 2.

Examples of globules are B163, B163-SW, B367 in the southeast and in particular B161 near the centre of the photograph. The latter appears as the cornerpoint of an angular-shaped dark lane, which reaches from the north to the projected centre of IC 1396, then getting narrower and running to the west, and it is best outlined as entry 161 in Khavtassi's (1960) atlas of dark clouds (see e.g. Fig. 12 of Kun 1986). Khav 161 contains a number of very dark condensations, e.g. Anon DC, Scho 1318, L1112, L1117, and perhaps L1128. Khav 155/156 traces diffuse dark material south of rim B, and adjacent to this, in the southwest of IC 1396, an extended dark complex exhibits more indistinct contours and includes B365, which appears as an reversed S, and B160. Also away from the line of sight to the H II region is L1086 in the west. Simonson & van Someren Greve (1976) and Tomita et al. (1979) conclude that the distance to several dark clouds in the vicinity of the IC 1396 region is 400 pc. Martin & Barrett (1978) also assumed a distance of 400 pc towards B163 and B163-SW. We shall adopt this value

Table 1. Observational parameters. The system temperature considers all atmospheric and instrumental losses, but the given errors are mainly due to the atmosphere. The last two columns give typical values. The r.m.s.-noise is that of the spectra which have been resampled to a spectral resolution of 0.21 km/s.

Telescope	Line and transition	HPBW	Positions observed	Grid	Resolution km/s	T_{sys} K	Integration time s	r.m.s.-noise K
Nagoya 4 m	^{12}CO (1→0)	2.′8	6050	2′	0.13	900 ± 150	21	0.73
	^{13}CO (1→0)	2.′9	5002	2′	0.08 and 0.135	800 ± 350	110 and 45	0.35
POM-2 2.5 m	^{12}CO (2→1)	2.′2	676	2.′5	0.20	3250 ± 470	570	0.40
			398	2′	0.20	2200 ± 380	215	0.45
	^{13}CO (2→1)	2.′3	82	2.′5	0.215	2950 ± 350	1020	0.25
			382	2′	0.215	1750 ± 200	385	0.23
KOSMA 3 m	^{12}CO (3→2)	1.′5	79	1.′25	0.145	3750 ± 950	250	0.60
			742	1′	0.145	2550 ± 600	21	1.20
	^{13}CO (3→2)	1.′3	45	1′	0.15	5150 ± 750	315	0.65
	C I (1→0)	1′	1		0.10	16000	3460	0.48
Effelsberg 100 m	H I (0→1)	9.′2	484	8′	0.32	48 ± 6	16	0.62

as well (see also Sect. 6.2). However, we note that a distance of 150 pc towards B161 was applied by Leung et al. (1982).

There are still some questions which need to be clarified:

The dark lane Khav 161, the dark globules, the B160/B365 complex and L1086 are thought to be not associated with IC 1396. However, located in front of the H II region, we may view them from the dark side not facing HD 206267, with possible bright rims pointing away from us.

The shell-shaped cloud system associated with HD 206267 might be interpreted as a remnant of a once much bigger molecular cloud complex which has given birth to HD 206267 and the B star cluster before being dispersed by the expanding UV/H II region and the strong winds of the young stars. Another possibility is that HD 206267 and Tr 37 are approaching a group of previously unrelated clouds driving a shell-type ionization front into them (Wendker & Baars 1980).

3. Observational data

The molecular line observations have been carried out with three small telescopes from three observatories in three countries. Both ^{12}CO and ^{13}CO were observed in the three lowest transitions. The J=1−0 large-scale mapping was essentially done with the 4 m telescope at Nagoya University (Japan). The J=2−1 mapping was performed with the POM-2 2.5 m telescope of Grenoble Observatory, located at an altitude of 2550 m on Plateau de Bure (France), and the J=3−2 observations were provided by the University of Cologne KOSMA 3 m telescope, located on Gornergrat (Switzerland) at 3200 m altitude. The 21 cm atomic hydrogen (H I) line was observed with the MPIfR 100 m telescope at Effelsberg (Germany). The observational parameters are summarized in Table 1. Finally, the CO and H I data will be compared with IRAS Sky Brightness maps.

3.1. CO *observations*

Our CO multi-line study comprises (before averaging) a total of about 19 000 individual spectra (including about 3000 spectra for calibration and pointing purposes). The largest amount of individual data is available for the (1→0) transition of ^{12}CO and ^{13}CO, with a total of more than 12 000 spectra.

1. Nagoya 4 m observations

The ^{12}CO (1→0) observations with the Nagoya 4 m millimeter wave telescope (Kawabata et al. 1985) were carried out in March and April 1990, the ^{13}CO (1→0) observations from November 1988 to February 1989, in May 1989, in December 1989/January 1990, and in March and April 1990. These observations (based on a preliminary large-scale ^{12}CO survey with the old Nagoya 1.5 m telescope, Y. Fukui, priv. comm.) were made in frequency-switching mode. In the 1988/89 winter, the 15 K cooled Schottky mixer receiver provided a receiver temperature (DSB) of 200 to 250 K at 110 GHz, and the 1024 channel acousto-optical spectrometer had a spectral resolution of 29.5 kHz (0.08 km/s). In the 1989/90 winter, an SIS receiver (Nb/Al-oxide/Nb−junction cooled to 4.2 K) exhibited a best noise temperature of about 25 K at 110 GHz. The 1024 channel acousto-optical spectrometer then had a spectral resolution of 49.5 kHz, covering a velocity range of −43 to +54 km/s in the folded spectra.

The gain of the Nagoya telescope depends slightly on elevation, and the intensity was rescaled (using spectra observed at Ori KL, whose peak T_R^* values were taken to be 65 and 10.5 K for ^{12}CO and ^{13}CO (1→0), respectively). The atmospheric opacity was determined from skydips. Typical values for τ were between 0.4 and 0.55 at 115 GHz and between 0.15 and 0.25 at 110 GHz.

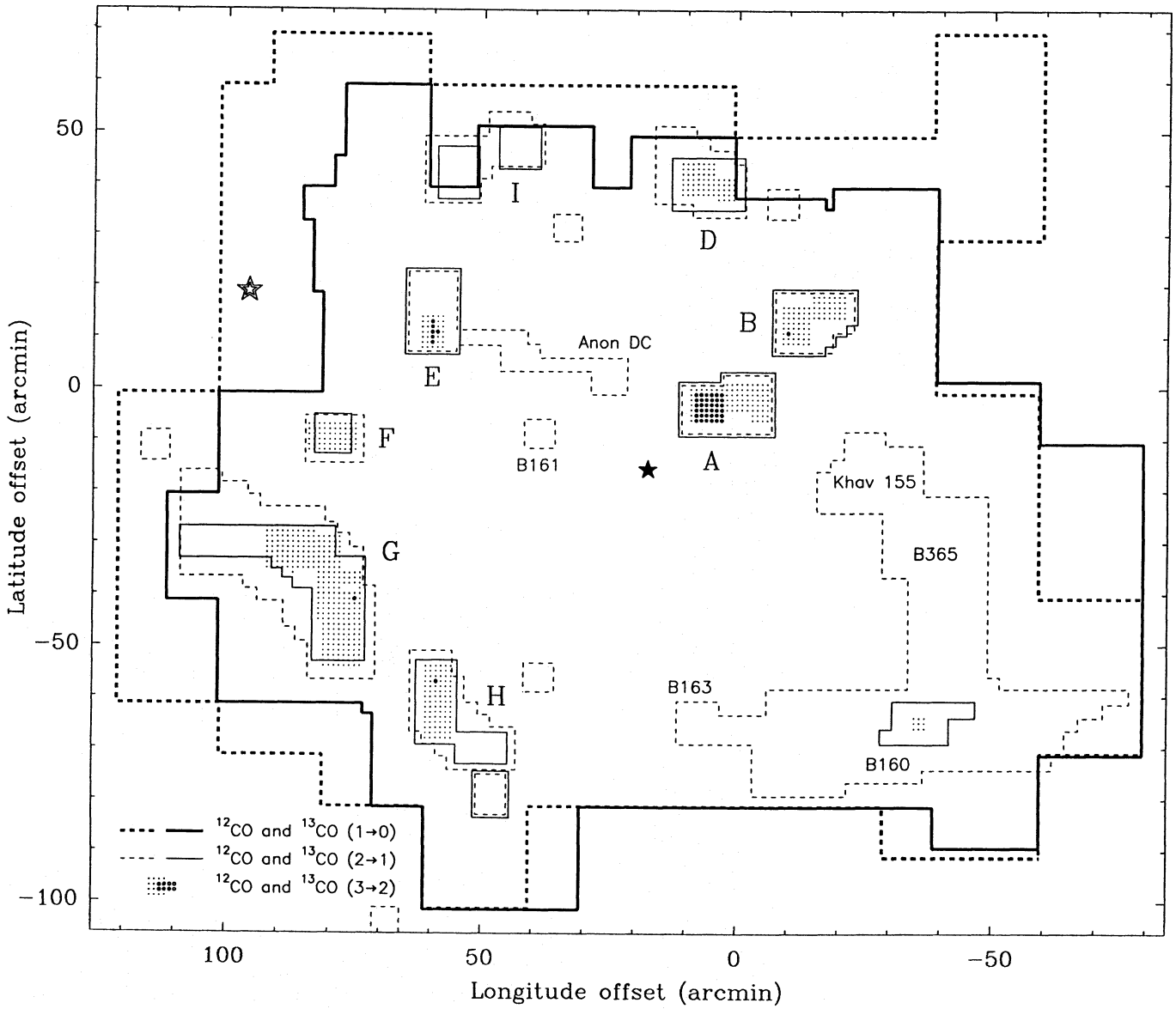

Fig. 3. Overview of the regions observed in the six CO transitions. (1 → 0) and (2 → 1) mapped areas are thick and thin lined, respectively, and dashed and solid polygons indicate ^{12}CO and ^{13}CO mapped areas, respectively. ^{12}CO (3 → 2) observations are shown by dots, and positions observed in ^{13}CO (3 → 2) are emphasized. For easy comparison with the finding chart (Fig. 2), some labels of bright-rimmed and other dark clouds are included.

2. POM-2 2.5 m observations

The ^{12}CO and ^{13}CO (2→1) observations were carried out with the POM-2 2.5 m millimeter telescope (Castets et al. 1988). Those made in winter 1988/89 (November to February) are on a 2.′5 grid (based on a preliminary undersampled large-scale ^{12}CO survey with the KOSMA 3 m telescope, see below) and cover essentially rim G and the B160/B365 complex, and those in winter 1989/90 (December to March) are on a 2′ grid and complete mainly for other bright rims. We used a Schottky diode mixer cooled to 15 K, which provided noise temperatures (DSB) of 250 to 320 K and 300 to 380 K at 220 and 230 GHz, respectively. The observations were made in frequency-switching mode using as backend a 256 channel digital autocorrelator with a spectral resolution of 156 kHz (0.21 km/s).

The POM-2 spectra were calibrated correcting for all atmospheric and instrumental losses when observed, using the chopper-wheel calibration procedure (Kutner & Ulich 1981) with a model to derive atmospheric transmission from its emission (Guilloteau 1988, Cernicharo 1985). The main beam efficiency is 63% (derived from Jupiter observations).

3. KOSMA 3 m observations

We made a preliminary undersampled large-scale ^{12}CO (1→0) survey with the KOSMA 3 m submillimeter radio telescope (Winnewisser et al. 1986) in May/June 1988: 237 positions

(HPBW of 3′.8, velocity range from −60 to +45 km/s) were observed on a 20′ grid centred at IC 1396, thus covering about 26 deg^2. The ^{12}CO (3→2) spectra of rim A (1′.25 grid) were obtained in total power mode in March/April 1989, and the spectra of rims B and D to H (1′ grid) in February/March 1990. The DSB noise temperatures of the Schottky mixer receiver (cooled to 20 K) were 520 to 600 K (Winnewisser et al. 1990). In March 1994 we obtained with the same receiver (but with T_{rec} improved to 380 K) a ^{13}CO (3→2) map (1′ grid) of rim A and observed also towards single positions in some of the other rims. In February 1993 we obtained with a Schottky receiver (T_{rec} (DSB) about 550 K) at a zenith optical depth of about 1.0 a spectrum of atomic carbon, i.e. the C I $^3P_1$–$^3P_0$ line at 492 GHz, towards one position in rim A. We usually used only 500 channels of the medium-resolution (167 kHz) 2048 channel AOS.

The KOSMA ^{12}CO (3→2) spectra have been corrected for atmospheric losses using the chopper-wheel method. Because of the relative sizes of beam and sources we adopt a beam efficiency of 55%: The measured beam efficiencies were 40 and 69% on Jupiter and Moon, respectively (Röhrig 1990). During the ^{13}CO (3→2) observations we derived efficiencies on Jupiter of 45% and on the Moon of 66%, and we used an efficiency of 55%. The 1993 efficiencies at 492 GHz were 13 (Jupiter) and 57% (Moon), and we adopted a value of 35%.

Fig. 3 presents an overview of the regions mapped in the six different transitions. The (1→0) observations (^{12}CO and ^{13}CO) cover the entire region of about 6 deg^2. The observations in the other transitions cover higher density regions, such as the bright-rimmed clouds, the B160/B365 complex in the southwest, some small clouds, and some IRAS point sources. The coverage of the bright-rimmed objects in the J=3–2 transition is not complete.

Because there are no strong northern hemisphere pointing sources (e.g. planets) near IC 1396, we regularly made small maps (1′ sampling) of the bright rim A, which is only 4′ in extent, in order to check pointing and calibration of the telescopes. The long-term pointing accuracy of the three telescopes was found to be somewhat better than about 25″.

All line temperatures are on the T_R^* scale (cf. Kutner and Ulich 1981). The absolute errors of our temperatures are estimated to be between 30% (for some Nagoya spectra observed at larger atmospheric opacities) and 20% (for all other spectra). However, relative errors, which have to be taken into account when line intensity ratios are compared, are much lower.

Loren et al. (1975) found a T_R^* of 24.2 and 5.6 K for ^{12}CO and ^{13}CO (1→0) at the centre of rim A using the MWO 4.9 m antenna. With the Nagoya telescope we obtained values of 19 and 5.8 K, respectively.

A similar cross-check of ^{12}CO (2→1) observations of rim A with KOSMA and POM-2 leads to a consistency of the calibration of the two telescopes within 10%: The intensity observed at POM-2 is somewhat lower, perhaps due to the lower spatial resolution.

We compared the calibrations of the three telescopes using the dark cloud B5, because of its simple line shapes (almost gaussian) and uniformity (we find less than 7% variation in peak and integrated intensity for both ^{12}CO and ^{13}CO (1→0) in 25 spectra in a 4 x 4 arcmin^2 region around RA(1950) = 3^{h}44^{m}28^s.7 and Dec(1950) = 32°44′30″):

With the KOSMA and the Nagoya telescopes we find in B5 at (0,0) a ^{12}CO (1→0) T_R^* of 12.7 K and with the Nagoya telescope we obtain a ^{13}CO T_R^* of 6.8 K. This is close to the values of 9.4 and 11.6 K for ^{12}CO and 6.3 K for ^{13}CO found by Langer et al. (1980) and Young et al. (1982) using the AT&T Bell 7 m telescope.

With POM-2 we get a T_R^* of 9.4 and 4.0 K for ^{12}CO and ^{13}CO (2→1), respectively, whereas Langer et al. (1980) and Young et al. (1982) report 8.1 and 4.2 K from AT&T Bell 7 m observations.

3.2. CO *data reduction*

After subtraction of a baseline and folding of the frequency-switched data, all spectra, which were not observed with POM-2 and possess higher spectral resolution (see Table 1), have been resampled to a velocity resolution of 0.21 km/s. Then, the spectra were stored in 9 data cubes (cf. Table 1). To allow a multi-line analysis, all data cubes have been smoothed to the largest beam size (2′.9) (assuming in all cases that there is no emission outside the observed regions) and resampled to the coarsest grid (2′.5).

We determined H_2 column densities N(H_2) first from ^{12}CO velocity-integrated T_R^* values W_{CO} using the averaged factor $X = N(H_2)/W_{CO} = 1.5 \cdot 10^{20}$/(cm^2 K·km/s) (Bhat et al. 1986, see also Solomon & Barrett 1991 and Brand & Wouterloot 1994).

The second method used to derive N(H_2) is by combining ^{12}CO and ^{13}CO data and assuming LTE (see e.g. Martin & Barrett 1978). We used Dickman's (1978) value for the ^{13}CO abundance, i.e. $N(H_2) = 5 \cdot 10^5\, N(^{13}CO)$.

In both cases the resulting masses were multiplied with a factor of 1.3 to account for He (cf. Hildebrand 1983 and Loren 1989). The sizes (and densities) of the clouds were derived from the number of positions above a certain level (see Sect. 4.2) assuming a spherical cloud.

To get estimates of virial masses M_{VT} (in $M_\odot$) we use the expression of the virial theorem (cf. MacLaren et al. 1988) for a simple spherical system

$$M_{VT} = k\, R\, \Delta v^2$$

for clouds with radius R (in pc) and line width Δv (in km/s). The constant k=160 accounts for a density distribution $\rho(r) \sim r^{-3/2}$ (cf. Gierens et al. 1992).

For the discussion of peak T_R^* ratios $\mathcal{R}$ we define abbreviations, e.g.

$$\mathcal{R}(1) = \frac{^{12}T_R^*\,(1\rightarrow0)}{^{13}T_R^*\,(1\rightarrow0)} \quad \text{and} \quad {}^{12}\mathcal{R}(32) = \frac{^{12}T_R^*\,(3\rightarrow2)}{^{12}T_R^*\,(2\rightarrow1)}$$

for the ^{12}CO/^{13}CO interisotopic and the ^{12}CO intertransitional case, respectively.

The intertransitional line ratios were analysed using escape probability (Stutzki & Winnewisser 1985) and LVG models (Goldsmith et al. 1983), which assume a spherical cloud with constant density, temperature, and CO abundance. For each value of the kinetic temperature T_{kin} between 4 and 50 K

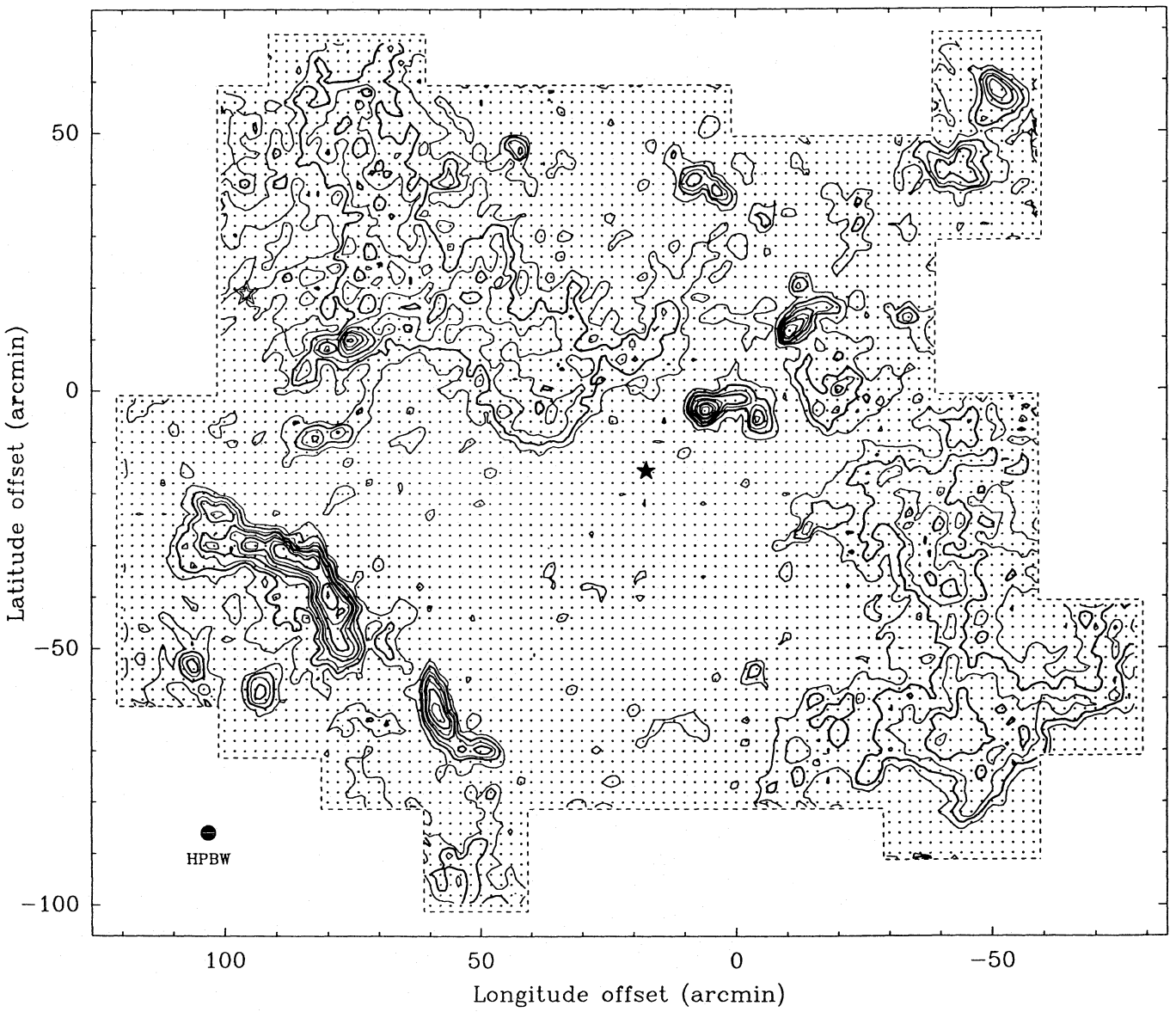

Fig. 4. Contour map of ^{12}CO (1 → 0) peak antenna temperature. The first contour is at 2.2 K (3σ-level), and the following contours are spaced by 1.5 K (2σ).

(in steps of 2 K) we varied $\log n_{H_2}$ in steps of 0.25 between 2 and 5 and $\log N(CO)/\Delta v$ in steps of 0.25 between 14.0 and 18.75; here n_{H_2} and N(CO) are the H_2 volume density and the CO column density, respectively. Comparing the observed and modelled line ratios for typical values of the peak temperatures, the combination of T_{kin}, n_{H_2} and $N(CO)/\Delta v$ with the lowest χ^2 was obtained. For the uncertainty in the T_R^* used for the χ^2 calculation we used a value of 0.5 K for ^{12}CO, and for that in the ratios, 0.05.

3.3. H I *data*

In August 1992 and January 1993 we have used the MPIfR 100 m radio telescope to observe the 1420 MHz H I ($^2S_{1/2}$,F=0−1) transition towards IC 1396. These 21 cm data cover an area of 3 x 3 deg^2. They were recorded in a 1024 channel autocorrelator, corrected for stray radiation and calibrated using the standard position S7 (Kalberla et al. 1982).

Column densities N(H I) are derived applying the factor $N(H\,I)/W_{HI} = 1.823 \cdot 10^{18}/(cm^2\,K \cdot km/s)$, assuming that the H I is optically thin.

3.4. IRAS *data*

For comparison with our CO maps we have used IRAS brightness maps at 12, 25, 60 and 100 μm covering 6 x 6 deg^2 centred at (l,b)=(99.0,+4.0), which have been prepared by IPAC (BIGMAP product). These are coadded survey data with 1′ pixels, which have been destriped, zodiacal light model subtracted, and smoothed to the 100 μm resolution of about 4′ in all

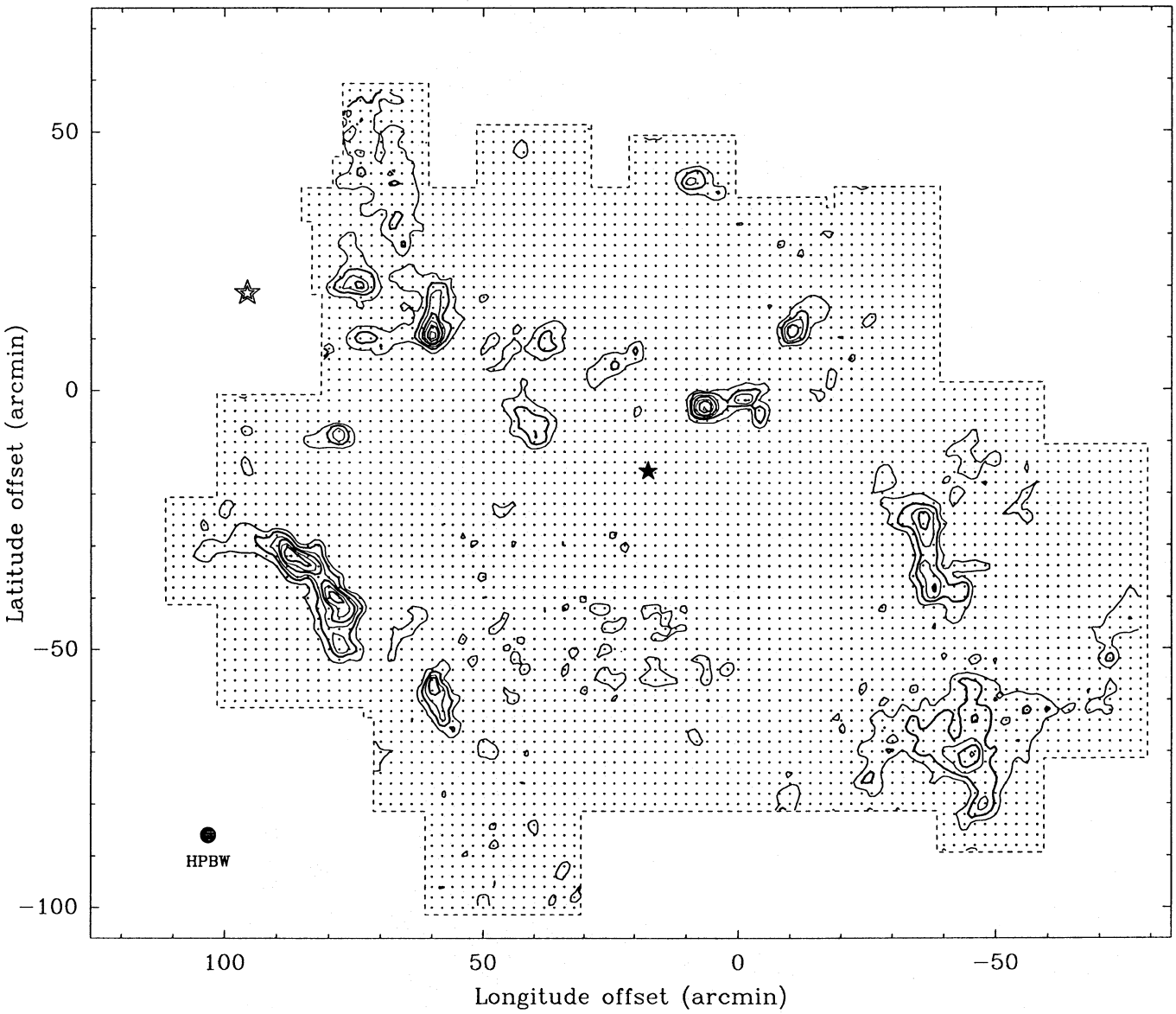

Fig. 5. Contour map of ^{13}CO (1 → 0) peak antenna temperature. The first contour is at 1.1 K (3σ-level), and the following contours are spaced by 0.7 K (2σ). Note that the contours between (0, −60) and (50, −40) are not real, but due to higher r.m.s.-noise in the spectra.

four bands. In addition, we used the second version of the IRAS Point Source Catalog (Beichman et al. 1988) to investigate the point sources in the region.

4. Results

4.1. Global structure of the region

4.1.1. Morphology

Contour maps of the peak T_R^* distribution for ^{12}CO and ^{13}CO are shown in Figs. 4 and 5, respectively. The complementary integrated intensity maps are not shown, but are very similar. The morphological aspects concerning the appearance of IC 1396 in IRAS brightness maps (see e.g. Fig. 11) are discussed in Sect. 5.1.

Comparing Figs. 4 and 5 to Fig. 1, one can see that (i) the ^{12}CO map excellently reproduces the outlines of all bright-rimmed features and of all other diffuse or dark clouds and globules and (ii) denser parts and cores, with high values of A_V, are well-traced by the ^{13}CO contours (see also Fig. 2). No CO emission is found in the vicinity of HD 206267, i.e. within a 1.5 deg^2 region around (25,−40). Therefore, the minimum in brightness on the optical photograph 25′ southeast of the O star is not caused by the presence of obscuring material.

The bright-rimmed clouds A, B and G show the most intense emission in both ^{12}CO and both ^{13}CO maps. The contours reveal the actual extension of the rim G cloud towards the east.

The cloud associated with rim E is very prominent only in ^{13}CO, shows even by far the strongest emission in the integrated intensity map, but is not seen in ^{12}CO due to strong

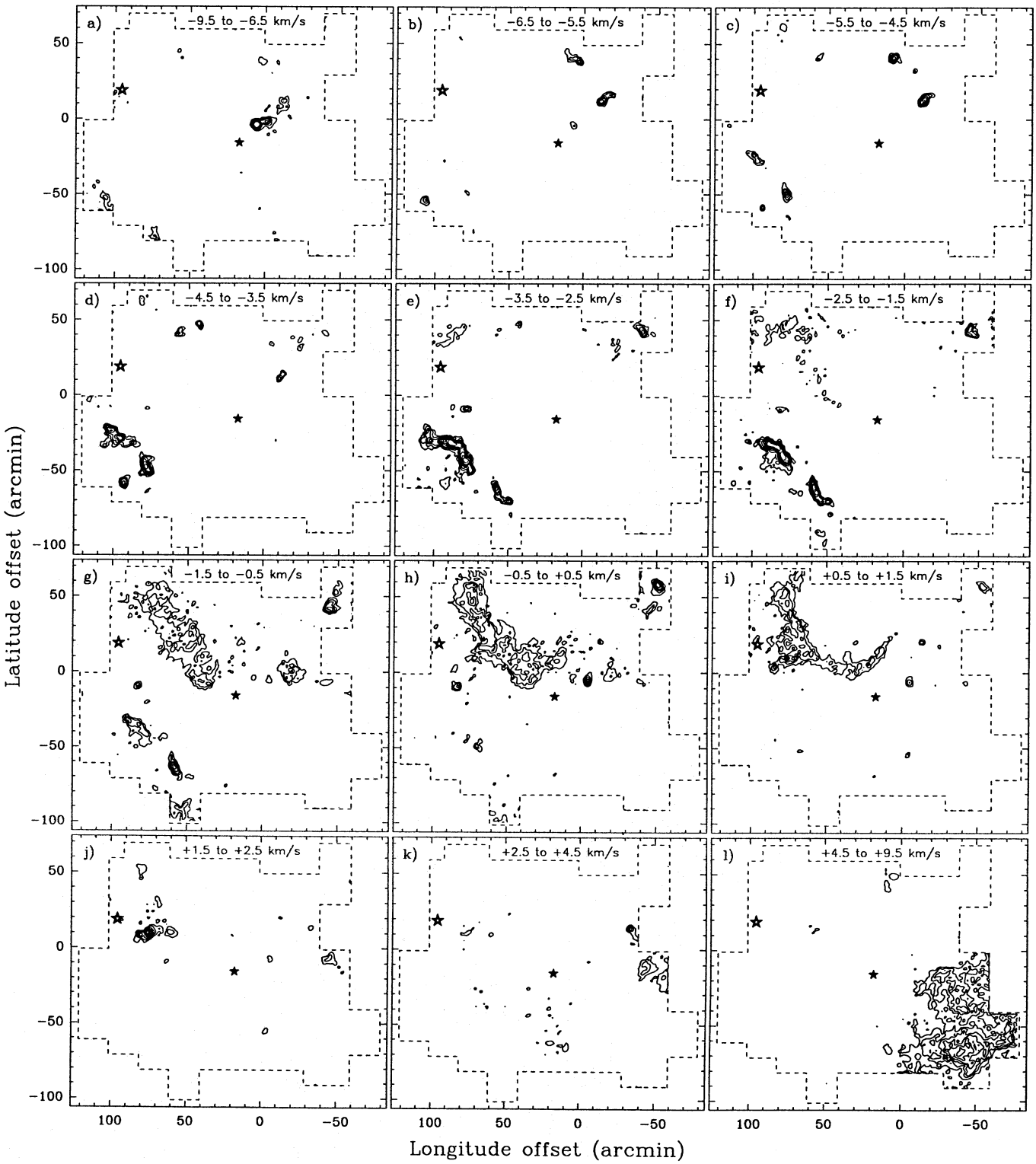

Fig. 6a–l. Velocity channel maps of ^{12}CO (1 → 0) integrated intensity. The first contour is at 2.2 K·km/s, and the contour step is 1.5 K·δv, where δv is the channel width or the average linewidth Δv (if $\Delta v < \delta v$). **a** to **f** mainly exhibit material associated with HD 206267, i.e. rims A and B, rim D, rim I and a fragment (field 47) probably eroded from the rim G cloud, rims G, F and H and L1086E, **g** to **i** contain associated (rim H, rim F E, rim Ab and the non-prominent rim E), probably associated (L1086W) and non-associated emission (Khav 161, Khav 155/156 and Khav 160), **j** shows rim Eb, **k** a probably associated small cloud (field 8), L1085 and B163, and **l** exhibits only foreground clouds (B160/B365).

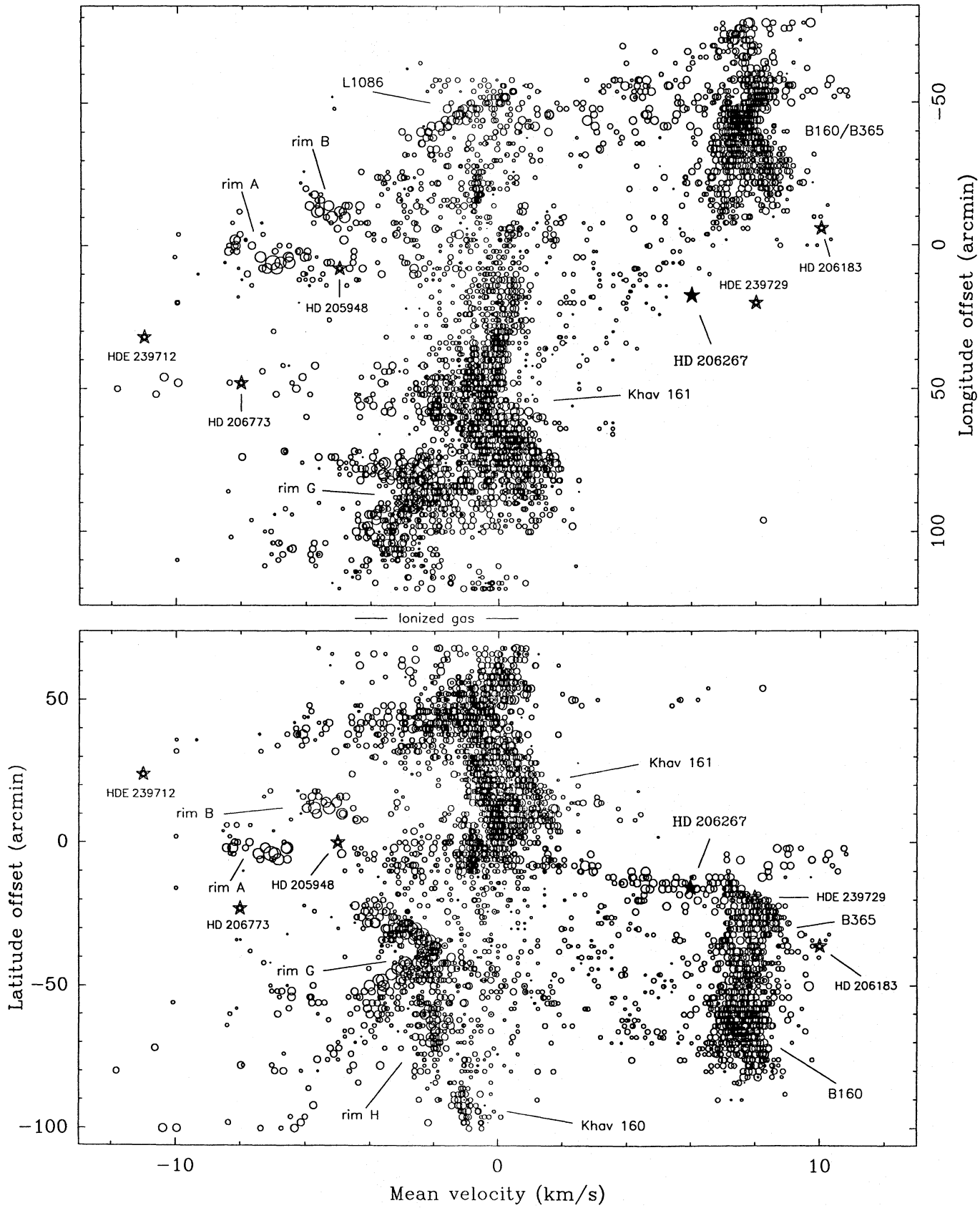

Fig. 7. Overview of the ^{12}CO ($1 \rightarrow 0$) velocity-position distribution. The abscissa "Mean velocity" represents the weighted mean of all emission features in the spectrum at each position. The size of the symbol is proportional to the integrated intensity. In addition, the radial velocity and position of some stars of earlier type than B3 are indicated. The velocity range occupied by ionized gas is given as well (Pedlar 1980).

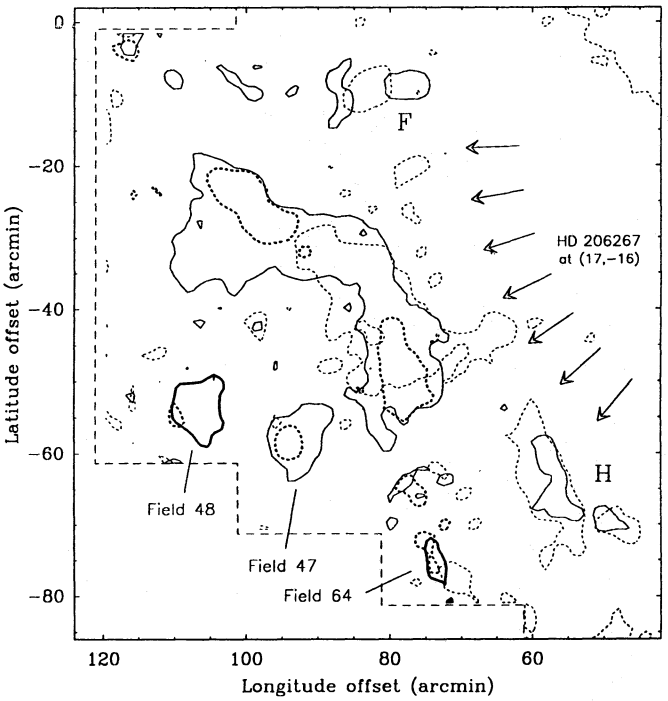

Fig. 8. Modification of Fig. 6 for the kinematics of rim G. The kinematic structure of the rim G cloud and the higher negative velocity of several cloud fragments exhibit an erosion process driven by the wind of HD 206267 (sketched by arrows) (see Sect. 6). The level at 2.2 K·km/s is drawn for four velocity intervals with a channel width of 1.4 km/s. Three contours show the distribution of blue-shifted material at −6.5 (solid thick-lined), −5.1 (dashed thick-lined) and −3.7 km/s (solid thin-lined). The reddest material is found at −0.9 km/s (dashed thin-lined).

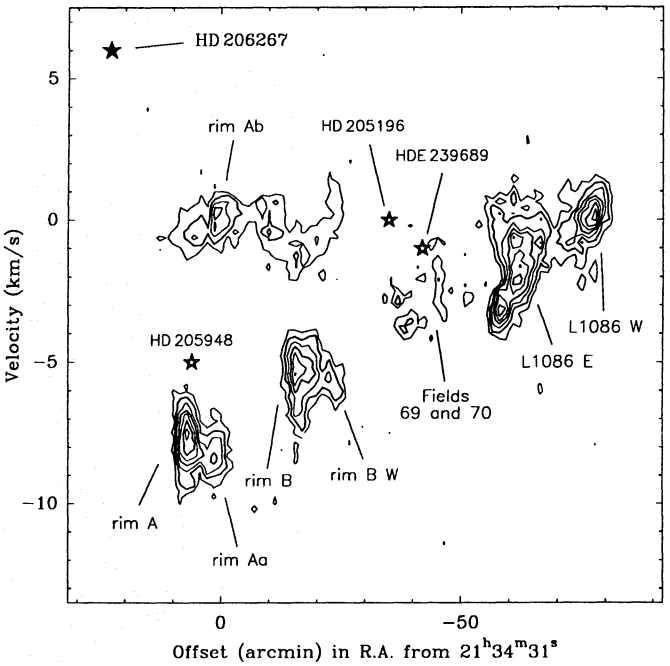

Fig. 9. ^{12}CO (1 → 0) position-velocity map integrated over all declinations in a stripe of 24′ width. The stripe is inclined by 45° with respect to (l,b), therefore the notation of (RA,Dec) is approximate (error about 3°). The first contour is at 0.95 K (3σ-level), and the contour step is 0.65 K. According to their radial velocity and position, loci are indicated for stars which are of earlier type than B3 and which are found in or close to the stripe. The clouds Aa and B W appear as wind-swept features of the rims A and B, respectively, and L1086E shows a velocity structure which probably traces a violent present or past (see Sect. 6).

self-absorption effects (cf. Sect. 6.1): The maximum at (58,16) in Fig. 4 is caused by the rim Ea cloud. The rim Eb cloud is clearly visible in the ^{12}CO maps, striking only in the peak T_R^* map due to relatively small line widths, and weaker in ^{13}CO (Fig. 5).

Due to the beam size of about 3′, the rim H clouds are far from being resolved: The ^{12}CO peak T_R^* map traces only the approximate outline of the four features Ha and Hb towards the north (not separated at all) and Hc and Hd towards the south (roughly separated). Only the cone feature Ha is remarkable in the ^{13}CO peak T_R^* map (Fig. 5).

The clouds associated with rims Aa, Ab, D, F and I are less conspicuous, but visible in all four maps and best traced in ^{13}CO integrated intensity and both peak T_R^* maps. Around the line of sight to rim C several faint components at various velocities have been detected only in ^{12}CO.

None of all these features reaches far beyond the outer perimeter of the H II region (cf. Fig. 1). The covered surface is at most 600 arcmin^2, i.e. the rim G cloud.

Contrary to this, other diffuse or dark clouds are rather widely extended. Fig. 4 outlines Khav 161 and the complex including B160, B365, L1085, and L1083, which certainly pass over the mapped region in the north and in the southwest, respectively. Fig. 5 traces denser parts and globules, e.g. B161, Anon DC, L1112, and L1128, and the cores which belong to B365 and B160.

The outlines of L1086 in the west, hardly visible on the photograph, are clearly exposed in the ^{12}CO map: Finally, we perceive two clouds, an eastern and a western.

Which of all these objects are really related to the H II region IC1396 is discussed in the following subsections.

4.1.2. Kinematics

For the study of the kinematic structure of the entire IC 1396 region, we prepared channel maps with spacings of one to several km/s, shown in Fig. 6. Fig. 7 gives an overview of the velocity distribution of the clouds along galactic longitude and latitude. A remarkable velocity structure (V-shaped in Fig. 7) is visible in the rim G region and highlighted in Fig. 8. In addition, we made ordinary position-velocity maps in smaller fields along four directions. Here, the most significant velocity gradients were found for the region from L1086 W to the rims B and A (see Fig. 9). Figs. 8 and 9 are discussed in more detail in Sect. 6.1. For comparison with these molecular data, we show in Fig. 10 six channel maps of the H I emission (combining some of the velocity intervals in Fig. 6).

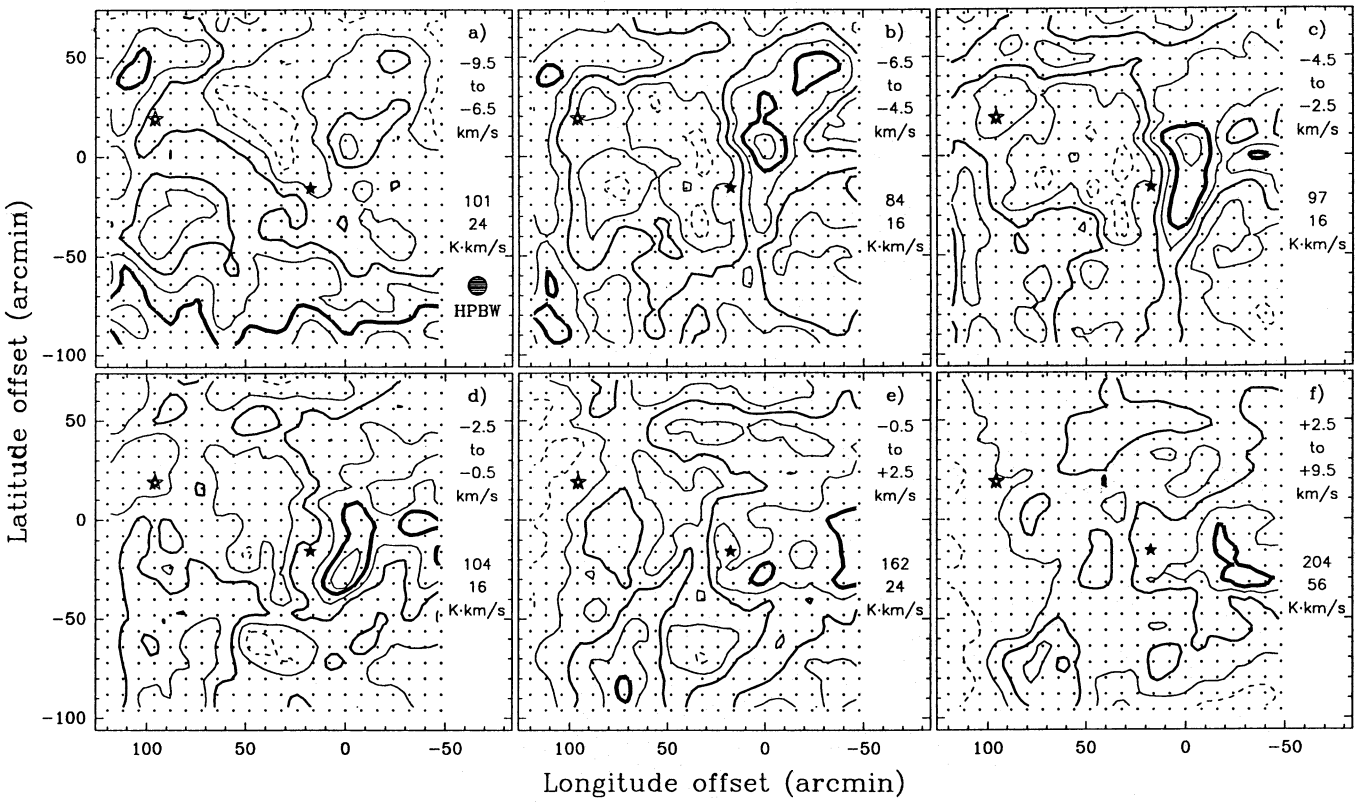

Fig. 10a–f. Velocity channel maps of H I integrated intensity. For each map the first contour level (dashed, 4 K·δv above the map's minimum) and the contour step (8 K·δv) are given. The third and fifth contour are thick-lined (with increasing weight).

The velocities of the bright-rimmed clouds are in a 10 km/s range between −8.3 and +1.7 km/s (see Figs. 6 and 7 and Table 2). In more detail, bright-rimmed clouds are found in Fig. 6 a at −8 km/s (rim A), in Fig. 6 b and c around −5.5 km/s (rims B and D and the most blue-shifted parts of rim G), in Fig. 6 d at −4 km/s (rim I and blue-shifted parts of rim G), in Fig. 6 e and f around −2.5 km/s (rims F, G, H, and also L1086 E), and in Fig. 6 j at +2 km/s (rim Eb). Fig. 6 g to i show in channels around 0.0 km/s emission from rims Ab, E (but very weak), Eb, F E, H, and also L1086 W, in addition to widely extended emission from other clouds.

Hence, CO emission towards normal dark clouds was detected in two distinct velocity ranges, i.e. (i) around 0.0 km/s, the Khav 161 broad dark (or diffuse) lane reaching from the north towards the centre of the field, then slightly westward (Fig. 6 g to i), and (ii) between +4.0 and +10.0 km/s, the B160/B365 complex in the southwest (Fig. 6 l).

In contrast to CO, there is H I emission at all positions and velocities (Fig. 10). However, in the velocity channels corresponding to those of most bright rims, −9.5 to −0.5 km/s (Fig. 10 a to d), there is a minimum in H I next to HD 206267, extended to northern directions by more than 1°. An H I maximum is seen towards the rims A and B (Fig. 10 a), being more prominent and elongated westward in Fig. 10 b, thus covering the rims C and D and L1086 E. This emission moves eastward in the following two channels, probably well-respecting the proximity of HD 206267 where a steep gradient is noticeable. Other emission, e.g. in the region of rims G and H in the same channels, is weaker, and one can distinguish no details because the resolution is only 9′. The maximum in Fig. 10 f is in the line of sight to the B365/Khav 155 complex and possibly associated with this.

4.2. Clouds

Based on our results (presented below), we regard a cloud as (possibly) associated with IC 1396 if we find at least two (only one) of the following four indications to be true: (i) the cloud appears bright-rimmed in Fig. 1, (ii) the observed antenna temperature ratio $^{12}\mathcal{R}(21)$ exceeds a value of about 0.6 (see Sect. 4.2.3), (iii) kinematic reasons favour an association with the H II region (see Sect. 4.1.2), or (iv) the cloud is in the line of sight to strong extended IRAS 100 μm brightness in Fig. 11 (see Sect. 5.1).

To analyse observed parameters, physical properties and line ratios within all clouds, we divided all positions with detected CO emission into 168 non-overlapping (elliptical) fields, each representing a separate cloud (or clump) or a part of a cloud in which the spectra have approximately equal velocities, shapes and line ratios $\mathcal{R}(1)$ (see Fig. 12): About 740 positions where the ^{13}CO (1→0) integrated intensity exceeds 1.8 K·km/s or the peak intensity is greater than 1.1 K are shown as filled circles, and open circles mark 665 positions where ^{13}CO is weaker than above, but where the ^{12}CO peak intensity exceeds 3.6 K. The

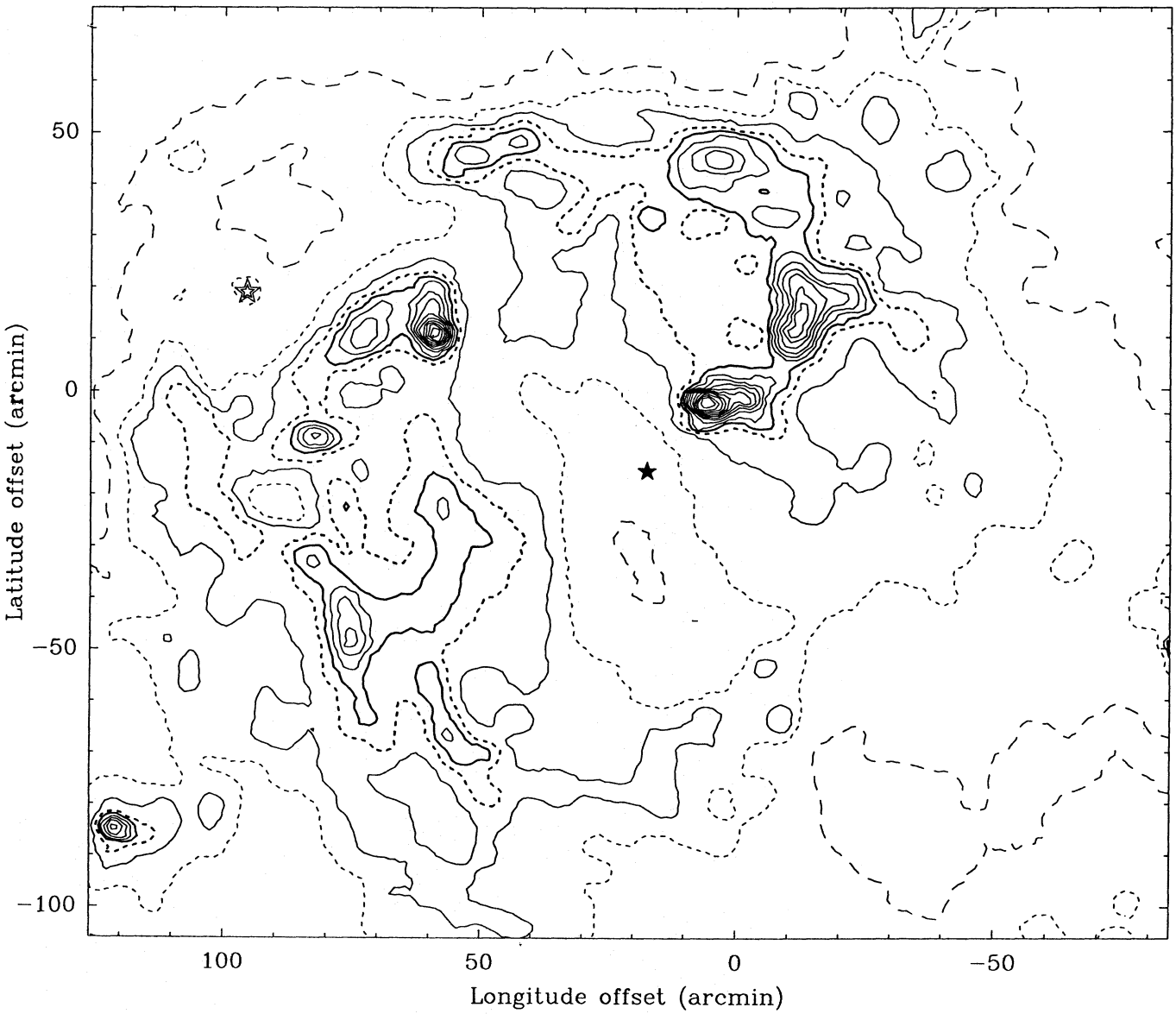

Fig. 11. Contour map of the IRAS 100 μm brightness (coadded map). Contour levels are drawn from 70 (thin long-dashed), 90 (thin short-dashed) to 350 MJy/sr, the step is 20 MJy/sr. Contours are thick-lined at 130 (short-dashed) and 150 MJy/sr (solid). The IRAS source X2152+574 at (120, −85) was not covered by our CO survey.

field numbers introduced in Fig. 12 are identified with cloud names in Tables 2 to 7 and in Sect. 6 as well.

Following the criteria (i) to (iv) from above we conclude that in Fig. 12 the fields 1 to 79 (thick-lined) are associated or possibly associated with the H II region, and the fields numbered from 100 to 188 (thin-lined) are probably not associated, but located in the foreground.

4.2.1. Line parameters

To deduce the observed ^{12}CO and ^{13}CO (1→0) parameters for clouds or parts of a cloud, we averaged the spectra in the fields of Fig. 12 and applied gaussian line fitting. The results are listed in Tables 2 and 3 for fields associated or not associated with IC 1396, respectively.

As already visible in Figs. 4 and 5, we observed the most intense ^{12}CO and ^{13}CO spectra towards bright-rimmed clouds. A comparison of the highest T_R^* values in Tables 2 and 3 shows that they differ by a factor of up to 1.5, keeping in mind that these are averaged values and that the field sizes in Table 3 are somewhat larger. However, the average Δv is a bit larger in Table 3, i.e. 2.0 vs. 1.85 km/s for ^{12}CO.

4.2.2. Masses

The densities and masses, derived from the average ^{12}CO and ^{13}CO line parameters within the (elliptical) fields using the

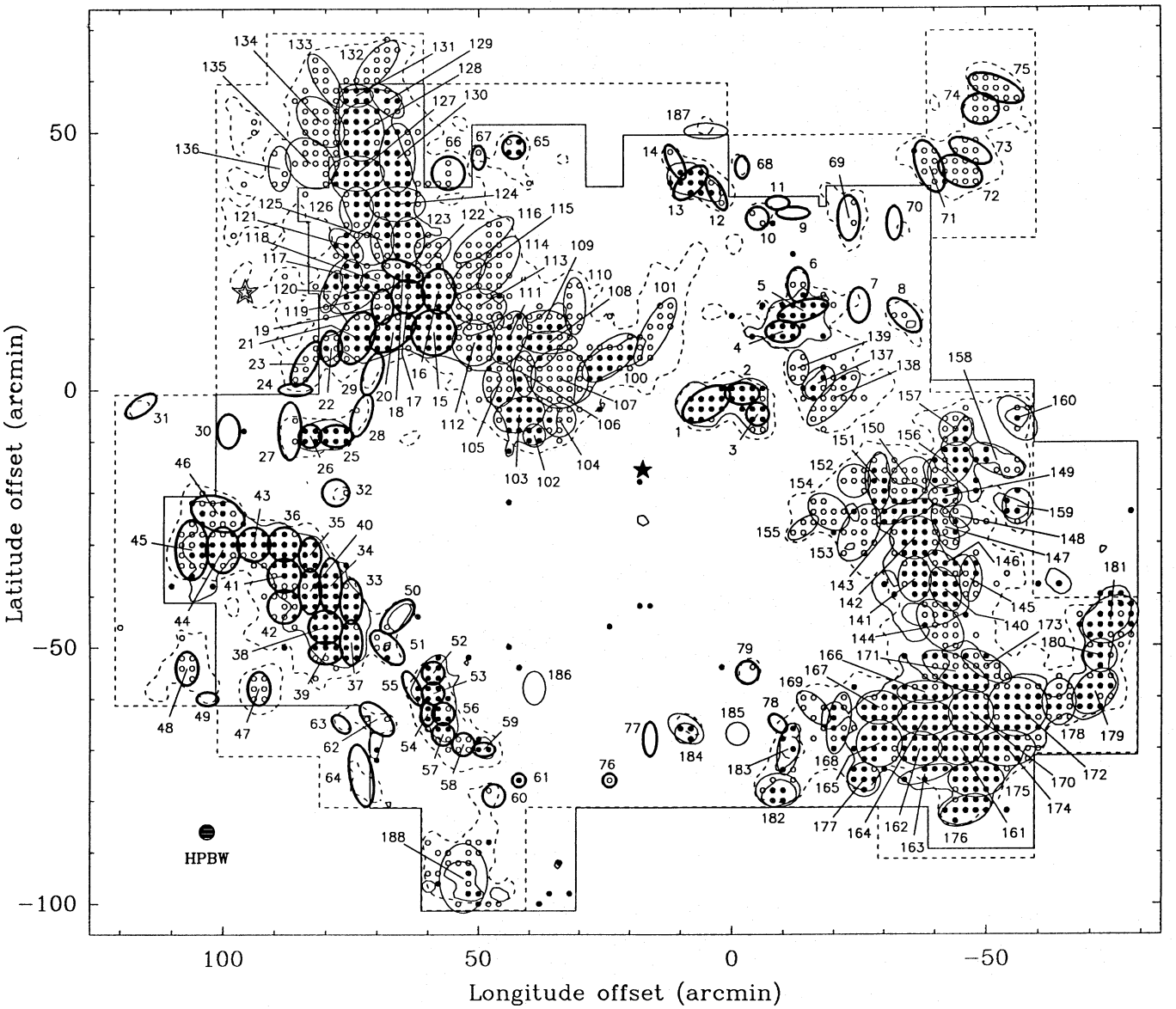

Fig. 12. Distribution of 168 elliptic fields where spectra have been averaged and gaussian line fitting has been applied to get observed parameters (Tables 2 and 3), derived densities and masses (Tables 4 and 5) and peak antenna temperature ratios (Tables 6 and 7). The limiting polygons and the first contours of the ^{12}CO and ^{13}CO ($1 \rightarrow 0$) maps (smoothed to a resolution of 2′.8 and 2′.9) are shown as well, dashed and solid, respectively. Filled circles indicate positions where ^{13}CO is easily detected, and open circles inside the solid polygon stand for ^{12}CO domination, i.e. absent or weak ^{13}CO emission (see Sect. 4.2 for details). Fields labeled with a 3-digit number (ellipses thin-lined) are regarded as not associated, all others (thick-lined) as associated with HD 206267.

methods mentioned in Sect. 3.2, are listed in Tables 4 and 5 for clouds associated or not associated with IC 1396, respectively.

In both tables typical densities n_{H_2} are between 300 and 700/cm^3, with core densities of 1200 to 1400/cm^3. Compared to the observed masses, virial masses are larger by a factor of almost 10, this factor being larger for smaller clouds (cf. Bertoldi & McKee 1992), with the noticeable exception of L1128 (see Sect. 6.2).

Our analysis leads to a total molecular mass associated with IC 1396 (including He) of about 3700 $M_\odot$, of which 1200 $M_\odot$ are found in ^{13}CO cores (cf. Table 4). These values can be compared with the ionized gas mass of 2900 $M_\odot$ (Matthews et al. 1980). We find for the cold dark clouds Khav 161, B365 and the B160/L1083 complex (which are not associated with IC 1396) masses of 700, 300 and 600 $M_\odot$, respectively (cf. Table 5), however, we note that Khav 161 and L1083 have not been observed completely.

From the H I data we have derived the mass of the atomic gas associated with IC 1396. This was done by integrating over the velocity range −9.0 to +2.0 km/s in intervals of 1 km/s. In each interval we subtracted the lowest intensity found in the map, assuming that this is a lower limit to the amount of fore-

Table 2. Observed ^{12}CO and ^{13}CO (1 → 0) parameters for selected clouds and cloud cores (or parts of clouds) associated or thought to be associated with IC 1396. Given are the field centre's offset from (l,b) = (99.0+4.0) (column 3), the corresponding equatorial coordinates (4), the number of positions in the field on the 2′grid (5), the ^{12}CO and ^{13}CO (1 → 0) line parameters obtained from gaussian line fitting of the averaged spectra (6 to 10), and the interisotopic line ratio $\mathcal{R}(1)$ (11). Entries in the last column indicate if (i) a significant displacement of the ^{13}CO velocity with respect to the ^{12}CO velocity has been measured or (ii) departures from gaussian line shape have been detected for ^{12}CO or/and ^{13}CO (classified from 2 to 9, with 2 almost gaussian and 9 highly departing from gaussian). Parentheses indicate poor determination. Note that for rim E the ^{12}CO T_R^* is only assumed (two times the value found in the fit, indicated by an asterisk) and that the related values Δv and $\mathcal{R}(1)$ could be doubtful.

No	Cloud	Offset arcmin	R.A. Dec (1950.0) h m s ° ′	Positions	^{12}CO v_{LSR} km/s	^{12}CO T_R^* K	^{12}CO Δv km/s	^{13}CO T_R^* K	^{13}CO Δv km/s	$\mathcal{R}(1)$	Remarks
1	rim A	5 −3	21 35 13 57 17.0	12	−7.9	7.5	2.3	2.5	1.5	3.0	2
					−0.4	2.3	1.5	< 0.17		> 13	
2	rim Aa	−2 −1	34 25 57 13.9	6	−8.32	5.2	2.0	2.1	1.4	2.5	
					−0.2	1.6	2.2	< 0.16		> 10	
	⋮										

The complete table is only available in electronic form at CDS via anonymous ftp 130.79.128.5 (see A&A **280**, E1 (1993)).

or background radiation, not associated with IC 1396. We obtain in this way a mass of 4800 $M_\odot$ (not accounting for He contribution). From low-resolution observations, Simonson & van Someren Greve (1976) derived an H I mass of 16 000 $M_\odot$ for the gas near IC 1396 (corrected to the adopted distance of 750 pc). Our H I mass is slightly larger than the H_2 mass and the H II mass. Including 1000 $M_\odot$ for stars of earlier type than B3 (Simonson 1968) in Tr 37, the region contains a mass of about 13 000 $M_\odot$.

4.2.3. Line ratios

Multi-line studies, or the measurement of intertransitional line ratios, e.g. of CO or CS, have become a well-established method to determine the physical conditions prevailing in molecular clouds, that is the excitation regime, i.e. the temperature, the density and the opacity within the given transition.

In the present study, the various ratios of the measured three lowest J transitions of ^{12}CO and ^{13}CO turn out to be very sensitive indicators and thus allow to discriminate between e.g. bright-rimmed and dense foreground clouds. For the former, all three different J lines of ^{12}CO (or ^{13}CO) are generally about equally strong, indicative of external heating, whereas for the latter the higher J transitions are successively weaker, thus indicating two distinctly different excitation regimes for the IC 1396 region: the warm rim and the cold foreground material.

The observed line intensities and shapes of the different transitions are compared for selected positions on almost all bright-rimmed clouds in Fig. 13 a to o and for a position on a dark cloud without bright rim in Fig. 13 p. For the bright rims the peak T_R^* values and line profiles of the three ^{12}CO transitions are equal within the errors for almost all observed positions. Only the (3→2) line appears to be somewhat broader in rim B and rim H. The clouds not associated with bright rims have been observed in the (3→2) transition only at a position in B160.

For about 580 positions we have determined the ratios $^{12}\mathcal{R}(21)$ and $^{13}\mathcal{R}(21)$, and in addition when possible, $^{12}\mathcal{R}(32)$. A summary of the average values of these ratios is given in Tables 6 and 7 for the clouds associated with IC 1396 and for those not associated, respectively. A typical statistical error for the averaged values is 0.05, and the systematic error is estimated to be also 0.05. Asterisks indicate if the statistical error exceeded 0.10 (due to (i) real effects like in the rim G cloud (see Sect. 6.1) and/or perhaps (ii) pointing errors, which are more important for the smaller clouds).

Two examples of our higher transition emission maps are shown in Fig. 14, i.e. towards rim A, the only cloud we mapped in six transitions, and rim G, the most extended bright-rimmed cloud. A comparison of the corresponding contours in both ^{12}CO maps reveals that the (2→1) and (3→2) spatial distributions are identical (in spite of the higher noise level in the latter), a fact which is supported by $^{12}\mathcal{R}(32)$ close to 1.0 almost everywhere on bright-rimmed clouds (see e.g. Figs. 13 and 18 or Table 6). The same is true for both ^{13}CO maps (available only for rim A).

Our multi-line study clearly reveals two distinct excitation regimes in which we can distinguish four different heating conditions (see Tables 6 and 7 and Figs. 13 and 17 to 19): First, we find the bright-rimmed clouds where (1) $^{12}\mathcal{R}(21)$ is about 0.9 near the rims and in some cases even above 1.0, thus indicating warm material, and (2) positions away from the bright rim exhibit somewhat lower line ratios $^{12}\mathcal{R}(21)$ of about 0.7. The reason is that the material is exposed to a nearby strong heating source. Second, we see (3) normal dark clouds and globules (without bright rims) which show line ratios $^{12}\mathcal{R}(21)$ and $^{13}\mathcal{R}(21)$ of about 0.45, thus typical for cold, but dense material, and (4) that very low line ratios $^{12}\mathcal{R}(21)$ (about 0.25) can be attributed to diffuse material in the line of sight, which has lower density and optical depth and resembles high-latitude clouds. This material is only exposed to the omnipresent interstellar radiation field.

Table 3. Same as Table 2, but for selected clouds and cloud cores (or parts of clouds) which are thought to be not associated with IC 1396.

No	Cloud	Offset arcmin		R.A. (1950.0) h m s	Dec (1950.0) ° ′	Positions	^{12}CO v_{LSR} km/s	^{12}CO T_R^* K	^{12}CO Δv km/s	^{13}CO T_R^* K	^{13}CO Δv km/s	$\mathcal{R}(1)$	Remarks
100-101		20	8	21 35 40	57 35.3	31	0.4	4.1	2.1	1.0	1.3	4.3	9 2
102	B161	39	−9	38 52	57 35.0	4	−0.75	5.4	1.5	2.4	0.9	2.2	
⋮													
As for Table 2													

In general, the same is true for the ^{13}CO ratios $^{13}\mathcal{R}(21)$, but these show a tendency to be somewhat lower than $^{12}\mathcal{R}(21)$.

Considering this, we are able to detect if a molecular cloud in the line of sight to IC 1396 is actually heated by the H II region, thus if it is associated with it or not. The IRAS brightness maps confirm these results (see Sect. 5.1).

Because of beam dilution, the use of measured peak T_R^* values as an indicator for the distance between the cloud and HD 206267 is problematic. However, peak intensity ratios like $^{12}\mathcal{R}(21)$ (or $^{13}\mathcal{R}(21)$) should be much more reliable. Therefore, we determined mean line ratios $^{12}\mathcal{R}(21)_{pk}$ for positions which are on or very close to bright rims in each bright-rimmed cloud. These ratios as well as the ^{12}CO peak T_R^* values can be found in Table 8.

Using simple radiative transfer models (cf. Sect. 3.2), we made an estimate of the mean kinetic temperature T_{kin} towards the bright-rimmed clouds. Compared to the peak T_R^* of single transitions, line ratios are much less affected by beam dilution and/or self-absorption effects. As parameters to be fitted we took either (i) the three ratios listed in Table 6, not taking into account any T_R^* or (ii) only the ratio $^{12}\mathcal{R}(21)_{pk}$ of Table 8, but accounting for the above effects by assuming a peak T_R^* of 15 to 20 K (cf. results from larger telescopes reported by Nakano et al. 1989 and Duvert et al. 1990) for all bright-rimmed clouds. The χ^2 (derived from (i)) had a minimum for T_{kin} >30 K (rim A), 15 to 20 K (rim B), 12 K (rim D), >20 K (rim F), >25 K (rim G), and 12 K (rim H). In view of all uncertainties (see below) we note that method (ii) led to similar results. The line ratios appear to be even more sensitive to densities: We find mean densities of 3000 to 5000/cm^3 in most cases, being considerably higher than those reported in Sect. 4.2.2. The fits are not very good in most cases, probably because of the assumptions used in the model (constant density clouds having a single T_{kin}), which are not realistic. In addition, the lines we observe are not necessarily excited at the same depth in the cloud. We consider these model results as preliminary. However, the relative values for T_{kin} between the different rims will probably be correct.

From CO (in some cases only ^{12}CO) multi-line studies of warm molecular clouds (Phillips et al. 1979, Martin et al. 1984, White et al. 1986, Castets et al. 1990) including modelling of line profiles or LVG techniques, it is concluded that due to heating by the ultraviolet radiation of nearby young stars or the ubiquitous interstellar (UV) radiation field outer low density regions of clouds are hotter than the shielded interiors. In the bright-rimmed clouds in IC 1396 these temperature gradients could be significantly enhanced. We note that the measured intertransitional line ratios on the rim G cloud show a systematic behaviour across the cloud (see Sect. 6.1).

We also tried to obtain estimates of T_{kin} for the clouds not associated with IC 1396, using average ratios, but could not obtain a significant value for T_{kin}. Probably this is because the clouds have lower optical depth, and lower limits to T_{kin} of 5 to 7 K are given by the typical peak temperatures of these objects. A ^{12}CO multi-transition study of the dark clouds B68 and B361 (Avery et al. 1987) reveals an excitation pattern similar to our results for clouds which are not associated with IC 1396, i.e. the observed peak intensity decreases systematically with increasing rotational quantum number J. As for the warmer clouds mentioned above, those data were interpreted by a kinetic temperature which increases from the core (6 K) to the edge (15 K).

A detailed discussion of intertransitional line ratios will be given in a forthcoming paper (Weikard et al., in preparation).

5. IRAS results

In this section we compare the IRAS brightness (Fig. 11) with the optical photograph (Fig. 1), our CO maps (Figs. 4 and 5) and radio continuum maps (Matthews et al. 1980, Wendker & Baars 1980). In addition, we discuss the properties of some IRAS point sources which indicate the presence of star-forming regions.

5.1. IRAS *extended emission*

A first IRAS (60 μm coadded) map of the IC 1396 region has been published by Schwartz et al. (1991). In this map there is still significant striping, in contrast to the 100 μm map in Fig. 11. We show only this map because the structures seen in the 12, 25, 60, and 100 μm maps are similar, except that e.g. the 12 μm map contains some point sources (probably stars) that are not seen at 100 μm. This suggests that there are no very large differences in dust temperature in IC 1396.

The similarity between Figs. 11 and 1 in the global appearance of IC 1396 is striking: We encounter at FIR wavelengths again the horseshoe-type structure, open to the south, and a min-

Table 4. Derived physical cloud parameters for clouds and cloud cores associated or thought to be associated with IC 1396 using the ^{12}CO and ^{13}CO (1 → 0) results of Table 2, assuming a distance of 750 pc, and applying standard analysis (see Sect. 3.2). Given are the diameters of the equivalent circular fields (corresponding with the number of positions in columns 5 of Table 2) (column 3), the average integrated line intensity and column density for ^{12}CO (4) and ^{13}CO (8), respectively, and the derived H_2 densities, masses (including a factor of 1.3 for He) and virial masses for ^{12}CO (5 to 7) and ^{13}CO (9 to 11), assuming spherical geometry. In order to account for a more concentrated ^{13}CO distribution, the derived values in the last three columns are based on a smaller diameter, i.e. 80% of the diameter in column 3. Parentheses indicate poor determination. Note that for rim E the ^{12}CO T_R^* is only assumed in Table 2 and that all derived values could be doubtful, e.g. the integrated intensity (marked with an asterisk).

				^{12}CO				^{13}CO			
No	Cloud	Diameter		$\int T_R^* dv$	H_2 Density	Mass	M_{VT}	$N(^{13}CO)$	H_2 Density	Mass	M_{VT}
		arcmin	pc	K·km/s	$1/cm^3$	$M_\odot$		$10^{15}/cm^2$	$1/cm^3$	$M_\odot$	
1	rim A	7.8	1.71	18.1	773	129	818	4.2	754	64	309
2	rim Aa	5.5	1.21	11.1	670	40		3.2	816	25	
⋮											
As for Table 2											

Table 5. Same as Table 4, but for clouds or cloud cores thought to be not associated with IC 1396 using the ^{12}CO and ^{13}CO (1 → 0) results of Table 3, assuming a distance of 400 pc, and applying standard analysis (see Sect. 3.2).

				^{12}CO				^{13}CO			
No	Cloud	Diameter		$\int T_R^* dv$	H_2 Density	Mass	M_{VT}	$N(^{13}CO)$	H_2 Density	Mass	M_{VT}
		arcmin	pc	K·km/s	$1/cm^3$	$M_\odot$		$10^{15}/cm^2$	$1/cm^3$	$M_\odot$	
100-101		12.6	1.46	9.2	457	48	519	1.2	243	13	156
102	B161	4.5	0.53	8.5	1186	6	93	2.3	1334	3	24
⋮											
As for Table 2											

imum 20′ southeast of HD 206267. A steep gradient in brightness can be seen on the northern side of IC 1396.

The IRAS map traces excellently all regions which have been found in our CO multi-line survey to show high inter-transitional line ratios:

All bright rims A to I are prominent in Fig. 11 with rims A, B and E brightest and rim C faintest. The appearance of the bright rims Eb and I is a further strong argument that these objects are of the same nature as the other bright rims. We note a small (about 5′) displacement between rim D in the CO and FIR maps, the FIR having its maximum at larger distance from HD 206267.

In some important details, however, the appearance of IC 1396 on the IRAS map is rather different from that in the CO maps (Figs. 4 and 5). The extended cold foreground clouds Khav 161 and the B160/B365 complex are not at all prominent in the IRAS maps, not even at 100 μm. On the other hand, a curved elongated intense structure around (60,−30), extended features in the northwest and south of rim A, emission around (40,25), and a narrower feature reaching from (40,−75) to (5,−65) are visible in all IRAS bands and do not have counterparts in the CO maps. However, these regions, which we shall call "dust ridges", are bright in Fig. 1 and in radio continuum maps. The latter show both large-scale and small-scale features, visible in 2695 MHz maps (Matthews et al. 1980, Wendker & Baars 1980) and in the 1415 MHz map of Matthews (1979) (for rims A and B), respectively.

In summary, some structures in the FIR maps are also seen only in those radio continuum maps and others mainly in the CO maps. The reason for these similarities and differences between the IRAS, radio continuum and CO maps probably is that in the IC 1396 region there is about an equal amount of ionized and molecular hydrogen (cf. Sect. 4.2.2), both of which contain heated dust. We note that anomalous dust has been detected towards IC 1396 (Clayton & Fitzpatrick 1987).

To investigate whether in the IC 1396 region there is any cold dust, the emission of which peaks at wavelengths larger than 100 μm, we followed the method of Laureijs et al. (1991): From both the 60 and 100 μm maps we subtracted a uniform background (the brightness level in each map at (20,−30), see Fig. 11) and constructed a difference map S(100)−S(60)/0.21, 0.21 being the average value of S(60)/S(100) in diffuse clouds. Regions with positive "emission" in this difference map contain colder dust than average. We find that near IC 1396 this is only the case for the foreground cloud B160, where the cold dust is found at the ^{13}CO peak.

The average ratio R(60/100) of the flux densities of the rims is significantly larger than 0.21 (cf. Table 8): It varies between

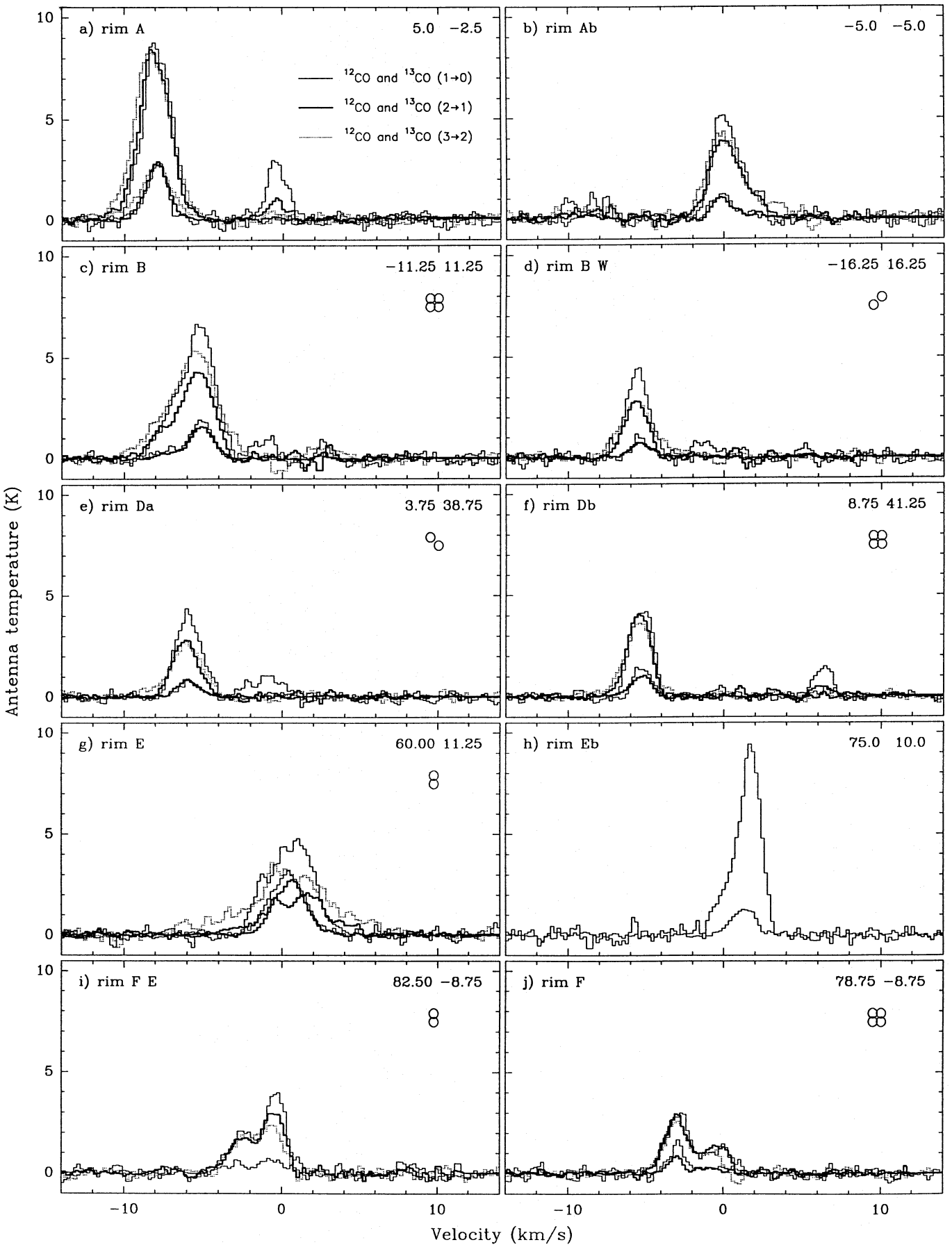

Fig. 13.

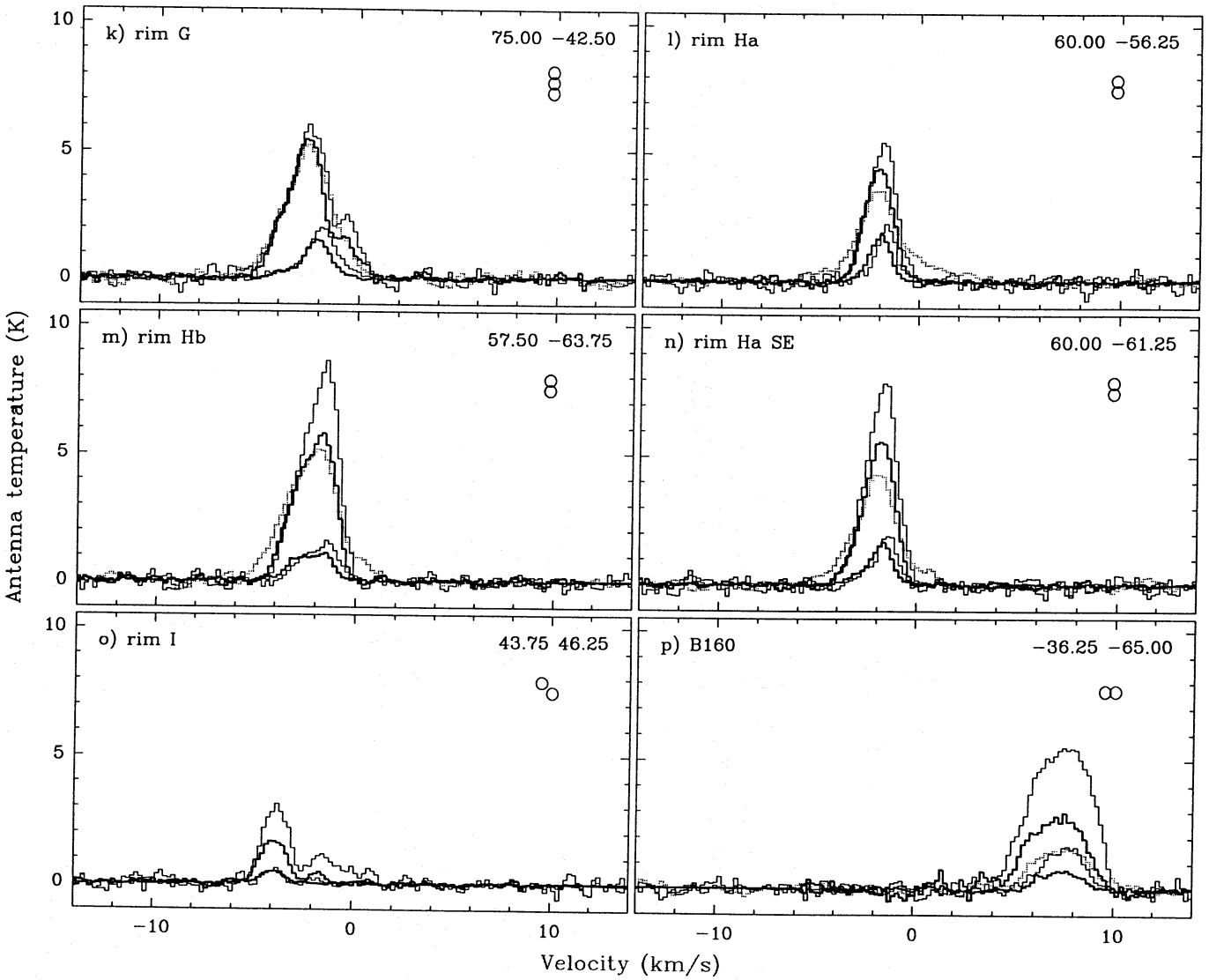

Fig. 13a-p. Comparison of line shapes observed with the three telescopes (spectra from the final data cubes: 2′.5 grid, 2′.9 spatial resolution, 0.21 km/s spectral resolution). ^{12}CO and ^{13}CO (1 → 0) are thin-lined, ^{12}CO and ^{13}CO (2 → 1) thick-lined, ^{12}CO and ^{13}CO (3 → 2) spectra dotted. The stronger set of three lines is due to ^{12}CO, the weaker to ^{13}CO. Note that for **g** rim E ^{13}CO (2 → 1) is more intense than ^{12}CO (2 → 1) and that not for all positions all six transitions have been observed, e.g. ^{13}CO (3 → 2) is available only for **a** rim A, for **h** rim Eb only (1 → 0) spectra have been observed, for **i** rim F E no ^{13}CO (2 → 1) and for **o** rim I no (3 → 2) spectra have been obtained. If spectra from several adjacent positions have been averaged, their arrangement with respect to the given offset is shown. **a** to **o** present spectra on clouds associated with bright rims, and **p** shows spectra taken on a dark cloud not associated with IC 1396.

0.29 for rim G to 0.47 for rim A, indicating that the dust temperature for rim A is highest, i.e. about 30 K (assuming a dust emissivity proportional to ν^2).

We calculated the FIR luminosity L_{rim} of the bright-rimmed clouds starting from background-subtracted maps in the four bands, integrating the brightness over the area A of the clouds (approximately given by the 150 MJy/sr contour in Fig. 11) and using the formula of Casoli et al. (1986). No corrections were made for contributions of point sources embedded in the rims (the highest luminosity point source, IRAS 21391+5802 in rim E, has an L_{FIR} of about 350 $L_\odot$, which is about 30% of the luminosity of rim E). These luminosities are listed together with other rim properties in Table 8. It is noticed that rims seen in projection close to HD 206267 tend to be brighter in the FIR, have a higher FIR colour temperature, and higher CO temperatures.

Assuming that the subtended areas of a rim are equal for HD 206267 and the observer and using the respective luminosities L_{star} and L_{rim}, we can roughly estimate the distance d between the rims and this star,

$$d = \sqrt{A \cdot L_{star}/(4\,\pi \cdot L_{rim})}\ ,$$

where A is the area as given above. Comparing HD 206267 to other O6.5V stars (Humphreys 1978), we adopt an absolute visual magnitude of $M_v = -5.2$ and a bolometric luminosity of

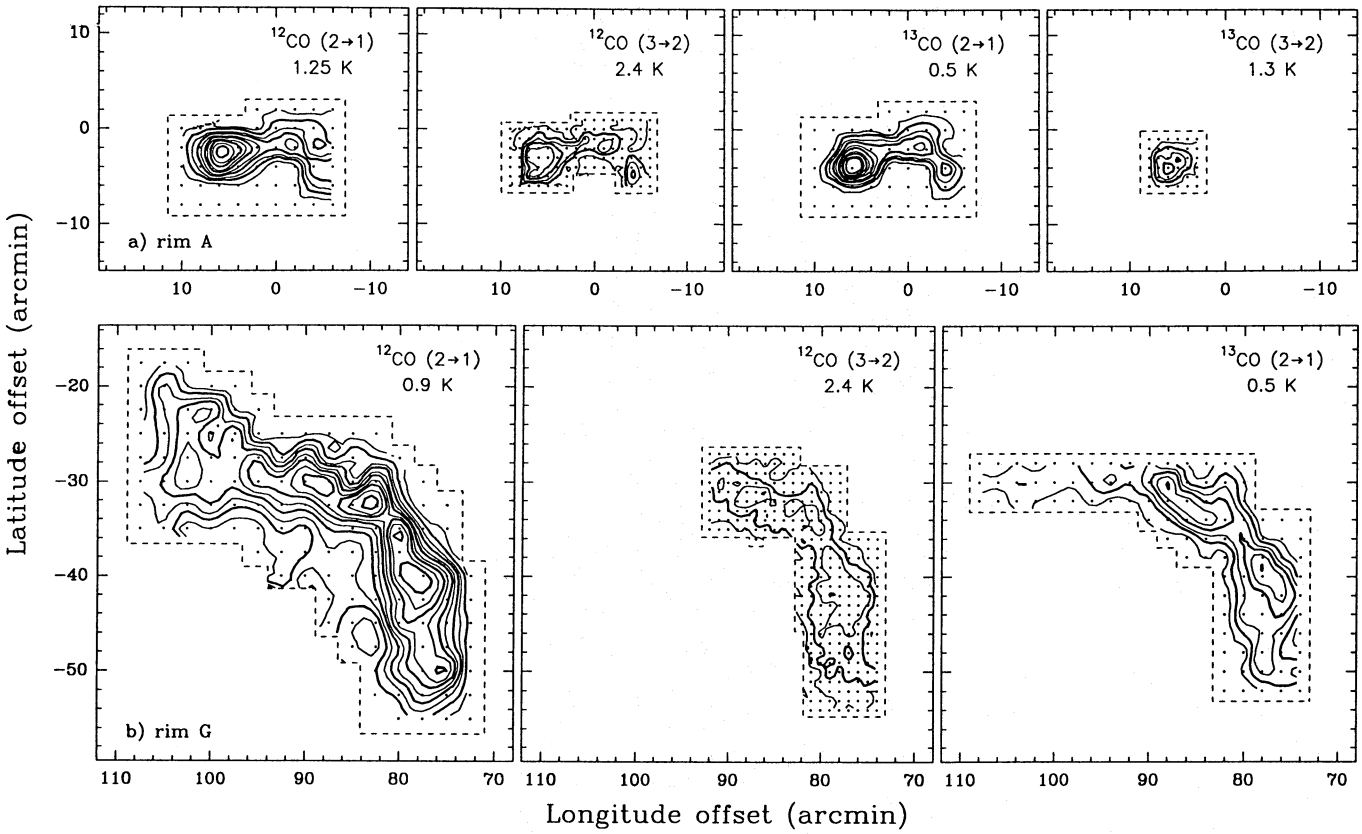

Fig. 14a and b. CO (2 → 1) and (3 → 2) contour maps of peak antenna temperature for rims A and G (cf. Figs. 4 and 5). The transition and the step (2σ) between two contour levels are indicated for each map. The first contour level is at 3σ.

$2{\cdot}10^5$ $L_\odot$ (cf. Blomme 1990, Garmany & Stencel 1992). In this way obtained distances d are of the order of 10 pc for all rims (cf. Table 8), and possible errors could be about a factor of 2: The distance d would (i) decrease for a smaller effective area as seen from the star (influence of wind) and an absorption of the star's radiation in the H II region and (ii) increase for other contributions to L_{rim} as from B stars or embedded point sources. Because of their optical appearance, we think that all rims are located slightly in front of HD 206267, with the possible exception of rims Ab, Ba and Eb. The total FIR luminosity within the IC 1396 region is $5.3{\cdot}10^4$ $L_\odot$, after background subtraction. Compared with the luminosity of HD 206267 this suggests that most radiation of HD 206267 escapes from the region.

5.2. IRAS *point sources*

The IRAS point sources near IC 1396 were studied already in detail by Kun & Pásztor (1990) and by Schwartz et al. (1991). Most point sources which were detected in 3 or more IRAS bands towards IC 1396 do not have the colours of star-forming regions, i.e. of Class I sources (cf. Lada 1987). Compared to Class I sources, they are warmer at 12 μm and colder at 100 μm, similar to the group 2 sources defined by Wouterloot & Walmsley (1986), which might be externally heated clumps.

Only few of the Class I sources are located in the bright-rimmed clouds and none of them in the brightest, rim A. The individual luminosity of the point sources is 350 $L_\odot$ or less (note that the values derived by Schwartz et al. (1991) from coadded data are about a factor of 1.5 larger than those derived by other authors). Two of these sources, IRAS 21388+5622 in rim J and IRAS 21391+5802 in rim E, show H_2O maser (see for both Gyulbudaghian et al. 1990 and Wouterloot et al. 1993) and CO outflow emission (Duvert et al. 1990, Sugitani et al. 1989), although the outflow in the former source has only a very low velocity. Three IRAS sources with colours of star-forming regions in IC 1396 were not detected in ^{12}CO (1→0) with the IRAM 30 m telescope by Wouterloot & Brand (1989): IRAS 21390+5634 [at (1,−55)], IRAS 21422+5625 [at (14,−80)], and IRAS 21426+5723 [at (55,−37)]. The first of these sources coincides within 8″ with the B star LS III +56°11 (Hardorp et al. 1964) of unknown spectral subtype. The other two lie towards extended FIR emission and are probably associated with this, but also might be background galaxies, which have similar IRAS colours as some star-forming regions. Based on a colour-colour diagram, Schwartz et al. (1991) suggested that IRAS 21445+5712, located in rim Ha, has T Tauri-like colours. However, this is not the case for the 12−25 μm colours, where it has the colours of other embedded stars (its luminosity is about 100 $L_\odot$). Fukui (1989) reports outflow emission towards this source. KOSMA ^{12}CO (3→2) mapping revealed an outflow source also towards IRAS 21320+5750 in rim Db (Sugitani & Ogura 1994). IRAS 21450+5658, located

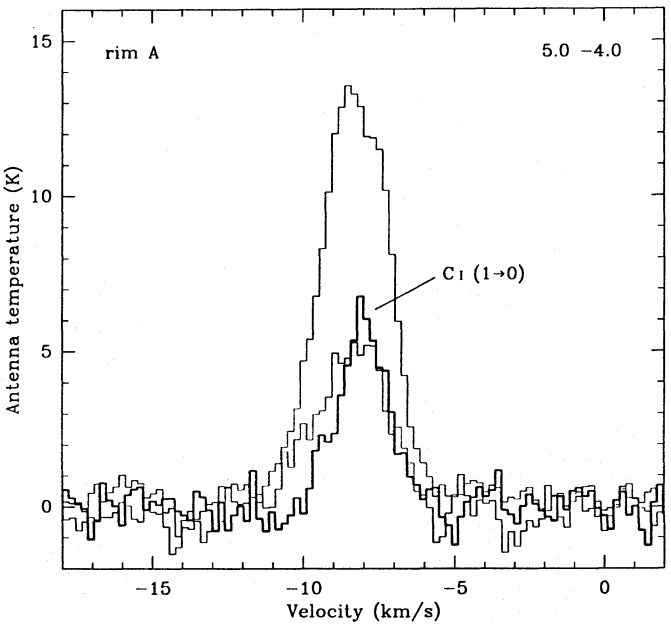

Fig. 15. C I spectrum for rim A compared with ^{12}CO and ^{13}CO (3 → 2). The spectra have been resampled to a spectral resolution of 0.21 km/s.

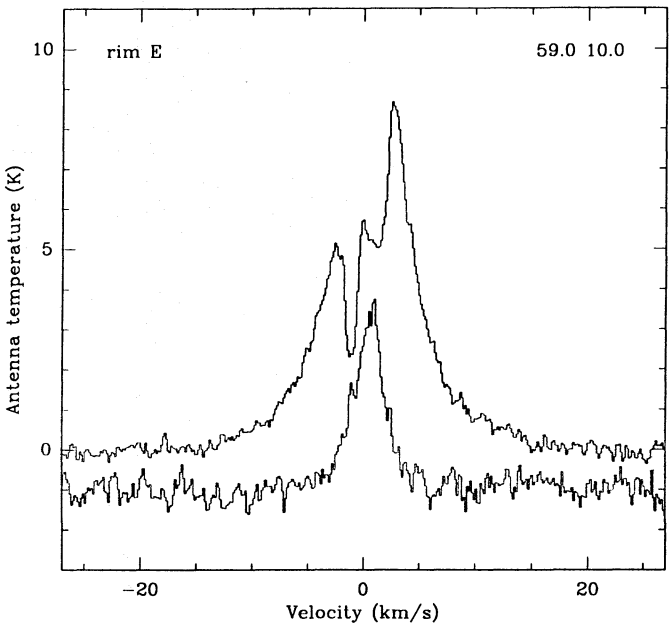

Fig. 16. Self-absorption in rim E as observed in ^{12}CO and ^{13}CO (3 → 2). The spectra are shown with their original spectral resolution of about 0.15 km/s (cf. Table 1). Note that the ^{13}CO spectrum has been shifted by −1 K.

in rim Hc, is the brightest CO source in the IC 1396 region detected by Wouterloot & Brand (1989), 21.7 K, but its colours are not those of maser-like regions (see Wouterloot et al. 1995), and it might be in an earlier evolutionary phase.

A more detailed discussion of IRAS point sources will be given in a forthcoming paper (Weikard et al., in preparation).

6. Details on the individual clouds

In the following we summarize the main properties of individual bright-rimmed (Sect. 6.1) and normal dark clouds (Sect. 6.2). The bright-rimmed and warmer clouds are associated with HD 206267, whereas the dark clouds are essentially foreground material, not associated with the IC 1396 material proper.

6.1. Clouds associated with IC 1396

Common to all bright-rimmed clouds is their enhanced temperature as determined by the line ratios $^{12}\mathcal{R}(21)$, $^{13}\mathcal{R}(21)$, and $^{12}\mathcal{R}(32)$ being close to 1.0 (see Fig. 13), indicating external heating by HD 206267. The former two line ratios decrease as one progresses away from the bright-rimmed area to the cloud's normal surface (especially in the case of rim G). Field numbers refer to Fig. 12 and Tables 2, 4, and 6.

Rim A: fields 1 to 3

Of all rims, Rim A is the brightest (^{12}CO (1→0) is 14.9 K), because it probably is the closest to HD 206267, which is located about 3.7 pc away in the plane of the sky. The CO emission (see Figs. 4, 5, and 14 a) matches almost exactly the cloud as it appears on the optical photograph (Fig. 1) and on the IRAS map (Fig. 11). In the spectra (Fig. 13 a) two velocity components at −7.9 and −0.4 km/s can be seen, but we attribute the latter to cold, optically thin foreground material, because the $^{12}\mathcal{R}(21)$ and $^{12}\mathcal{R}(32)$ ratios are only 0.3 and 0.15, respectively. For the main component (−7.9 km/s) the peak intensity ratios of the three ^{12}CO lines and the three ^{13}CO lines are very close to 1.0, indicating that the corresponding gas has been shocked and heated by the expansion of the H II region. The profiles of the main component are identical within the experimental uncertainty for all three ^{12}CO and ^{13}CO lines.

Fig. 15 depicts the ^{12}CO and ^{13}CO (3→2) spectra at offset (5,−4) together with the spectrum of the C I line at 492 GHz. It is seen that C I is as strong as the ^{13}CO (3→2) (or all other ^{13}CO lines, see Fig. 13 a), though the line width seems slightly smaller. Due to observational constraints we observed the C I transition at only one position, which is located in the centre of the extended radio continuum emission of rim A in the 1415 MHz map of Matthews (1979) (at $21^{h}35^{m}18\overset{s}{.}4$, 57°16′17″). Therefore, the C I emission probably originates from a PDR at the backside of the rim A cloud.

The rim Aa is even brighter than rim A on the optical photograph and shows a slightly higher negative velocity of −8.3 km/s. Since it is turned away from HD 206267, the rim Aa cloud could be a wind-swept feature (cf. Figs. 6 a and 9).

The rim Ab cloud seems to be illuminated at the frontside (see Fig. 1), and because its velocity is considerably different from that of rim A, i.e. about 0.0 km/s (Fig. 13 b), it is most probably behind HD 206267. The line ratio $^{12}\mathcal{R}(21)_{pk}$ of 0.77 ± 0.03 is based on two measurements.

Table 6. Peak antenna temperature ratios for fields associated or thought to be associated with IC 1396. Given are the velocity of the component (column 3), and the four measured ratios for those fields where the relevant transitions were available (4 to 7). A value is put in parentheses if only 1 or 2 positions were available. It is indicated if components are not associated (na) or lines are self-absorbed (sa) or have not been detected (nd). For more details see Sect. 4.2.3.

No	Cloud	v_{LSR} km/s	$^{12}\mathcal{R}(21)$	$^{13}\mathcal{R}(21)$	$^{12}\mathcal{R}(32)$	$^{13}\mathcal{R}(32)$
1	rim A	−8.0	0.72*	0.92*	1.24*	0.87*
		−0.5 na	0.40	nd	0.46*	nd
2		−8.0	0.84	0.79	0.92*	
		0.0	0.68	0.83*	0.87*	
3		0.0	(0.76)	(0.86)	(1.04)	
4-5	rim B	−5.0	0.66	0.79	1.17	
		−7.0	0.75*	0.55*	1.40*	
9	rim C	−3.0	(0.65)			
11		−7.5	(0.45)			
12	rim D	−6.0	0.72	0.95*	0.85*	
		−1.0 na	0.20			
13-14		−5.5	0.95*	0.71*	0.90	
		6.5 na	0.33			
15	rim E	0.5	sa	0.82	sa	
16		−0.5	0.42 (sa)	0.93		
17 SW		0.0	0.48 (sa)	0.85*		
25-26	rim F	−3.0	0.91*	0.53	0.95*	
		−0.5	0.91*	(0.85)	0.82	
33	rim G	−2.5	0.89*	0.69	(0.93)	
34		−2.5	0.83*	0.60*	0.90	
35		−2.5	0.79*	0.67*	0.93*	
36		−2.5	0.70*	0.60	0.97	
37		−3.0	0.76	0.65	0.92	
		−0.5	0.57		0.95	
38-39		−3.5	0.66	0.55	1.00	
40-41		−2.0	0.55	(0.53)		
42 W		−2.0	0.62			
43-44		−3.0	0.58	0.68		
45-46		−3.5	0.62	(0.60)		
52	rim H	−2.0	0.78	(0.76)	(0.73)	
53		−2.0	0.74	0.72	0.82	
54		−1.5	0.69	(0.82)	(0.77)	
56-57		−2.0	0.63	0.66	(0.90)	
58		−2.0	0.69	(1.50)		
59		−2.5	0.74*	(1.07)		
		−0.5	0.42			
60		−2.5	(0.91)	(0.94)		
65	rim I	−4.0	0.65*	0.82*		
		−1.5 na	(0.28)			
66		−4.0	0.60*			
		−1.5 na	0.18			

Table 7. Same as Table 6, but for fields which are thought to be not associated with IC 1396.

No	Cloud	v_{LSR} km/s	$^{12}\mathcal{R}(21)$	$^{13}\mathcal{R}(21)$	$^{12}\mathcal{R}(32)$
100 SE		0.5	0.42		
102	B161	−0.7	0.41		
106+111 Centre		0.0	0.38		
140	B365	7.5	0.47		
141-143		8.0	0.43		
144		8.0	0.50		
145-146		7.5	0.43		
147-148+149 SE		7.5	0.37		
150 N		7.5	0.40		
151-152		7.7	0.44		
161-162+163 NE	B160	7.5	0.45		
164		7.5	0.46	0.41	(0.57)
165		7.5	0.47		
166-167		7.0	0.38		
168		7.5	0.47		
169		7.5	0.59		
170+172+174		8.0	0.40		
171+173 N		8.0	0.46		
177 NW		8.0	0.56		
178+179 SE	L1083 E	8.5	0.37		
		6.8	0.29		
182 W	B162 N	7.0	0.47		
183		7.0	0.70*		
184 W	B163	4.5	0.47		
185	B163-SW	5.0	(0.72)		

Most of the published work on IC 1396 has been done on the molecular cloud associated with rim A. Loren et al. (1975) conclude from CO observations that a temperature enhancement may be due to an embedded infrared heating source. Some early ^{12}CO multi-transition observations of this cloud revealed strikingly similar (1→0) and (2→1) line profiles and intensities (Plambeck et al. 1977). Wootten et al. (1983) studied the behaviour of various parameters (peak and integrated intensities, column density, line intensity ratios, velocity structure etc.) for the rim A globule using strip maps of several CO lines at 30″ resolution. One result is a dip in the ^{13}CO integrated intensity at the position of the late F star LkHα 349 (Dibai 1969, Herbig & Rao 1972). High-resolution CO observations (Nakano et al. 1989) reveal a cavity in the central part of the globule. Schmidt (1974) and Schwartz (1985) derived typical electron densities of about 1000/cm^3 for rim A, which is of the same order as the H_2 densities in Table 4, as one might expect. An average emission measure of about 3000 pc/cm^6 has been calculated for the rims A and B assuming an electron temperature of 10^4 K (Matthews 1979). Only the bright rims A and B show an intensity enhancement in the large-scale radio continuum maps (Matthews et al. 1980, Wendker & Baars 1980). Baars & Wendker (1976) and Matthews (1979) obtained radio continuum maps at 6 and 21 cm and discuss as well the possibility of an additional heating source (likely a B1 star).

Rim B: fields 4 to 7

Rim B, which appears brightest on the optical photograph, is somewhat less bright than rim A in CO. The rim A and rim B globules are of about the same size (diameter of about 1.5 pc) and contain nearly the same mass (about 100 $M_\odot$). In contrast to rim A, the ^{12}CO and ^{13}CO line shapes are asymmetric towards rim B due to a second component at −6.5 km/s, whereas the velocity of the main peak is −4.9 km/s (see Fig. 13 c). The profiles in the western part of rim B are symmetric (Fig. 13 d). Rim B is the only source in our survey where $^{12}\mathcal{R}(32)$ is significantly larger than 1.0, i.e. about 1.15, indicating that the rim

material is particularly warm, while $^{12}\mathcal{R}(21)$ and $^{13}\mathcal{R}(21)$ are both about 0.8.

As the rim A cloud, the rim B cloud, too, is elongated with rim B W turned away from HD 206267 (cf. Figs. 6 b and 9).

The rim Ba cloud is bright in Fig. 1, like rim Ab, has a velocity close to that of the latter and is probably also behind HD 206267. No ^{13}CO was detected.

Possibly due to beam dilution, the rim Bb cloud shows only weak ^{12}CO emission.

A small cloud (field 8) at +3.1 km/s is regarded as probably associated with IC 1396, because it is situated in the line of sight to strong extended FIR emission.

Rim C: fields 9 to 11

With typical upper limits for the masses of 10 $M_\odot$ or less, the rims C and D constitute next to the rim J cloud the smallest cloudlets in our survey. This is evidence that they are being destroyed by the action of HD 206267. Only very weak ^{12}CO (1→0) emission of about 2 K was detected in the line of sight to rim C at about −2.8 km/s. Emission at −4.5 km/s was detected northeast of rim C at the position of a faint bright-rimmed globule (rim Ca) and at −7.5 km/s northwest of rim C at the position of a tiny trunk-shaped globule (field 11). The latter globule is also detected in ^{12}CO (2→1).

Rim D: fields 12 to 14

Two CO emission peaks (Fig. 13 e and f) are detected towards the two globules known as rim D: The velocities are slightly different, i.e. −5.8 (the southern one, rim Da) and −5.25 km/s (the northern one, rim Db). For the smaller rim Da cloud $^{12}\mathcal{R}(21)_{pk}$ and $^{13}\mathcal{R}(21)$ are 0.72 ± 0.03 and about 0.95, respectively. For the rim Db cloud these values are interchanged, i.e. the peak T_R^* of the three ^{12}CO transitions are equal, e.g. $^{12}\mathcal{R}(21)_{pk}$ is 1.00 ± 0.06, while $^{13}\mathcal{R}(21)$ is about 0.7.

6.1.1. Rim E: fields 15 to 17

The clouds associated with rims E and Ea, at +0.4 and −0.4 km/s, are situated in the line of sight to Khav 161 which is found at the same velocity, i.e. −0.3 km/s. Although both rims are clearly visible in Fig. 1, and Khav 161 seems to be only diffuse (high $\mathcal{R}(1)$), a confusion with this foreground gas can not be excluded.

All ^{12}CO lines are heavily self-absorbed, this being even more pronounced in the higher transitions (see Fig. 13 g): Fig. 16 shows ^{12}CO and ^{13}CO (3→2) spectra at one position in the rim E cloud. In ^{12}CO (3→2) there appear to be two absorption features at different velocities (at −1.2 and +1.1 km/s), but from the ^{13}CO (3→2) spectrum it cannot be determined whether there are two separate absorbing clouds, although the slight asymmetry in the ^{13}CO profile at the peak may indicate the presence of two velocity components.

In the ^{12}CO (2→1) and (3→2) spectra we see also the red and blue wings of an embedded outflow which has been found from higher resolution observations by Sugitani et al. (1989), Wilking et al. (1990), and Serabyn et al. (1993). The strong self-absorption features are most probably caused by an embedded heating source (associated with this outflow), making the cloud core considerably warmer than the envelope, and it is less probable that the rather diffuse foreground gas of Khav 161 is responsible.

Fields 16 (rim Ea) and 17 show no clear self-absorption feature, but it is suspected to be present because of a high $^{13}\mathcal{R}(21)$.

Rim Eb: fields 19 to 22

The molecular cloud associated with rim Eb appears bright on the photograph (Fig. 1), thus probably illuminated at the frontside and located behind HD 206267. The relatively high interisotopic ratio $\mathcal{R}(1)$ indicates rather warm, but less dense material (cf. Fig. 13 h).

The fields 23, 24 and 28, 29 are rather weak in CO, but in view of their velocities, they might be disappearing "bridges" between rim Eb and the rim F component at about 0.0 km/s.

Rim F: fields 25 to 27

Two well-separated velocity components (Fig. 13 i and j) are associated with IC 1396, but only that one with the higher negative velocity (−2.95 km/s) is associated with rim F proper, while the other component (at −0.4 km/s) belongs to a small dark cloud reaching from rim F northeastward by about 6′: For both clouds we find high $^{12}\mathcal{R}(21)_{pk}$, 0.97 ± 0.07 and 1.00 ± 0.13, respectively, however we note rather large statistical errors. $^{13}\mathcal{R}(21)$ is substantially lower. We observed distinctly lower line ratios $^{12}\mathcal{R}(21)$ on the most northern position (82.5,−7.5) for both components, i.e. 0.76 and 0.64, respectively (see also Fig. 13 i), indicating warm gas, but not as warm as in the southwest near the rim. A similar, but clearly more pronounced dependence of $^{12}\mathcal{R}(21)$ on the position within a cloud has been found for rim G (see below).

The fields 30 and 32 are small diffuse clouds, probably dissipating into the interstellar medium. L1132 (field 31) is certainly somewhat more extended to the west (cf. Fig. 1). Due to its velocity of −4.4 km/s, we consider L1132 as probably associated with IC 1396.

6.1.2. Rim G: fields 33 to 46

The most extended molecular cloud in IC 1396, L1129 is associated with the two bright rims named G and Ga. The cloud is slightly bow-shaped, pointing with its tip toward the O star, with a north−south elongation of 10.5 pc and covering about 600 arcmin^2. The CO emission of the rims G and Ga appears about equally strong, whereas the 100 μm emission of rim G is much brighter than that of rim Ga. All along this ridge the ^{13}CO line peaks at −2 km/s while the ^{12}CO velocities are found to be between −4.0 and −1.0 km/s with the higher negative velocities appearing both at the northern and southern bow edges (Fig. 8). The ^{12}CO and ^{13}CO spectra in Fig. 13 k suggest the presence

Table 8. Comparison of further properties of the bright-rimmed clouds. Given are the projected distance between HD 206267 and the maximum of the FIR emission (column 2), the ^{12}CO (1 → 0) peak antenna temperature (3), the line ratio $^{12}\mathcal{R}(21)$ determined on bright rim positions (4), the area of the cloud occupied in the FIR (5), the FIR luminosity (6), which is also normalized (7), the ratio of the flux densities at 60 and 100 μm (integrated over the rims) (8), and a simple estimation of the distance between HD 206267 and the object (9). For more details see Sects. 4.2.3 and 5.1. Note that for rim D the extended FIR emission does not coincide with the molecular fields which lie 1 pc eastward and that for $^{12}\mathcal{R}(21)_{pk}$ the first three entries do not include values for rims Ab, Ba and Bb, and Ca, the values for rims D and F (marked with asterisks) average each two separate clouds (see Sect. 6) and those for rims C and I are based on only one measurement.

Rim	d_p	$T^{*,12}_{R,pk}(1\rightarrow0)$	$^{12}\mathcal{R}(21)_{pk}$	A		L_{rim}	L_{rim}/A	R(60/100)	d
	pc	K		arcmin^2	pc^2	$L_\odot$	$L_\odot$/arcmin^2		pc
A + Aa + Ab	3.7 – 5.2	14.9	0.90 ± 0.04	195	9.25	2000	10.3	0.47	8.8
B + Ba + Bb	8.8 – 11.3	12.9	0.69 ± 0.03	330	15.70	3000	9.1	0.42	9.3
C + Ca	11.8	4.5	(0.65)	99	4.70	600	6.1	0.37	11.4
(D)	13.2	(7.6)	0.86*	249	11.85	1800	7.2	0.38	10.5
E + Ea	10.6 – 11.4	sa		139	6.60	1200	8.6	0.35	9.6
Eb	13.1	13.1	no	131	6.20	900	6.9	0.33	10.7
F	14.0	7.0	0.98 ± 0.06*	52	2.50	400	7.7	0.34	10.2
G + Ga	14.1	14.4	0.92 ± 0.04	259	12.30	1700	6.6	0.29	11.0
H	12.6 – 13.8	11.9	0.84 ± 0.02	106	5.05	650	6.1	0.32	11.4
I	15.0	7.5	(0.80)	98	4.65	700	7.1	0.38	10.5

of self-absorption at about −1.5 km/s. As for rim E (see above) this self-absorption may be due to an embedded heating source, or to the fact that the part of the cloud directed to the observer is colder than the backside which is heated by HD 206267. However, in the latter case one might also expect similar effects towards rims A and B, which are not seen. Fig. 14 b shows the higher transition emission mapped towards rim G.

The multi-line observations result in the following: $^{12}\mathcal{R}(21)$ and $^{13}\mathcal{R}(21)$ are both close or equal to 1.0 at positions on the bright rim and become systematically lower towards positions with increasing distance from the rim. This systematic behaviour of the intertransitional line ratios in the rim G cloud is shown in Figs. 17 to 19. Fig. 17 presents a ratio map for $^{12}\mathcal{R}(21)$, which decreases from about 1.0 at the side facing HD 206267 to about 0.6 at the opposite side of the cloud. Spectra along a strip through rim G can be found in Fig. 18. Apart from the distinctly changing ratios $^{12}\mathcal{R}(21)$ and $^{13}\mathcal{R}(21)$, there is a difference in radial velocity between ^{12}CO and ^{13}CO, which is particularly large at offset (80,−40). This might be caused by the self-absorption seen also in Fig. 13 k. Fig. 19 summarizes our results for the characteristic behaviour of the three line ratios on all measured positions: The average ratios $\mathcal{R}(21)$ decrease with distance from the rim for both ^{12}CO and ^{13}CO, with $^{13}\mathcal{R}(21)$ significantly lower, while $^{12}\mathcal{R}(32)$ is rather constant. The fact that the increase of the ratio towards the rim is gradual might be caused by the limited angular resolution of the underlying (1→0) data: Steeper gradients are not visible, but smoothed.

The escape probability model (using the observed intertransitional line ratios along the strip in Fig. 18) gives a minimum χ^2 for the following kinetic temperatures: T_{kin} is larger than 35 K at (80,−32.5) (the minimum χ^2 is at 46 K, although its exact location is not well-determined), and for the next positions (80,−35) and (80,−40) we find T_{kin} values of 20 and 12 K, respectively. At the last position the fit to the observed ratios is not very good. For the same reasons as above (Sect. 4.2.3) these results are only preliminary. However, it is clear that within a region of 2.′5 from the rim, corresponding to 0.5 pc, the temperatures are significantly higher than on positions further away.

The small clouds (fields 47 to 49) behind the rim G cloud are found at somewhat higher negative velocities (see Fig. 8). They are probably eroded fragments from the bow-shaped rim G cloud, which obviously suffers from an ongoing erosion process (Whitworth 1979) directed by the wind of HD 206267.

Rim H: fields 52 to 59

The complex, highly fragmented structure named rim H comprises at least four small globules (cf. Figs. 1 and 2), which we call rims Ha through Hd. The velocity of the cone-like object Ha (Fig. 13 l) in the north is −1.6 km/s, and the ^{13}CO lines are displaced with respect to ^{12}CO (Fig. 13 n). Going further to the south we find higher negative velocities up to −2.6 km/s (Fig. 13 m). $^{12}\mathcal{R}(21)$ and $^{13}\mathcal{R}(21)$ are somewhat lower than 1.0, indicating warm gas.

Field 60, a small cloud, is almost certainly related with the rim H globules, because of its radial velocity of −2.4 km/s and high line ratios $\mathcal{R}(21)$ of about 0.9. Field 61 is the tiny globule GRS 23 (Gyul'budagyan 1986, Schwartz et al. 1991), which is clearly detected in our data, however far from resolved by the (1→0) beam. Fields 62 to 64 appear as dissipating fragments eroded from a formerly larger rim H cloud.

Rim I: fields 65 to 67

We find the individual globule associated with rim I (field 65) far to the north at a velocity of −3.7 km/s. $^{12}\mathcal{R}(21)$ and $^{13}\mathcal{R}(21)$ are 0.65 and 0.85, respectively, and indicate a cooler environment, probably due to the greater distance from HD 206267. The ^{12}CO line profiles (Fig. 13 o) show secondary components at −1.5 and around 0 km/s, which are attributed to Khav 161 and

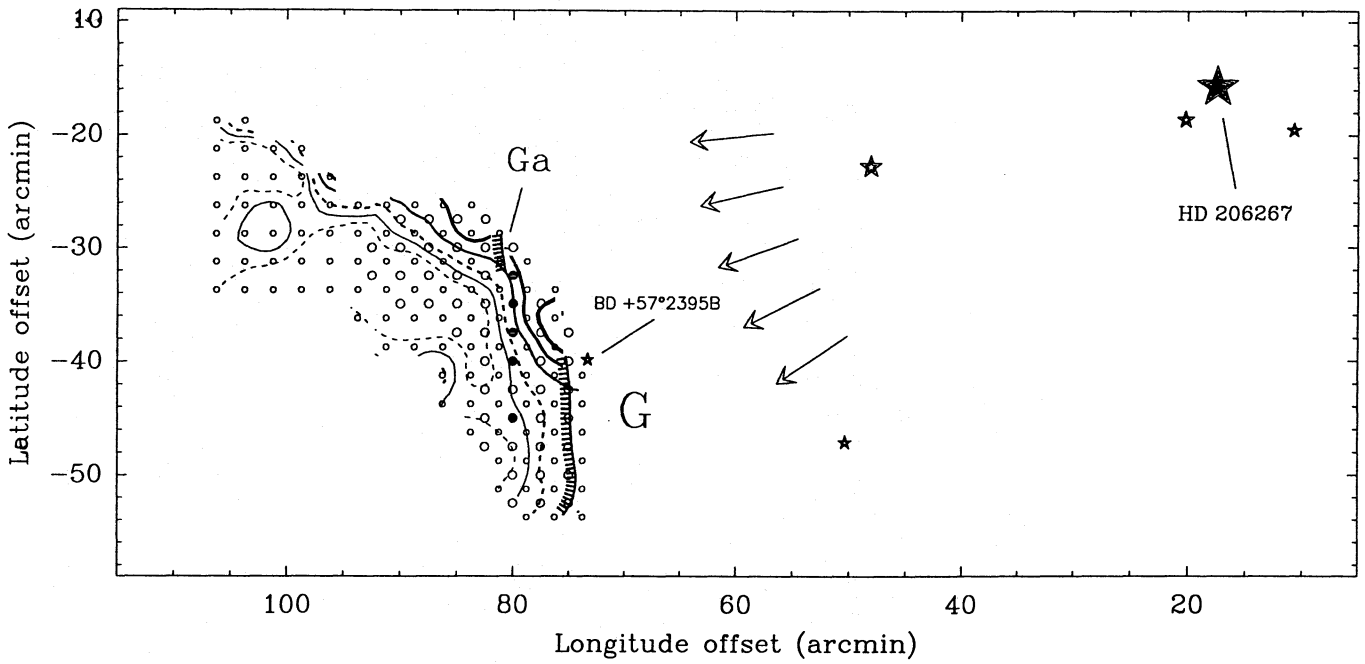

Fig. 17. Contour map of observed ^{12}CO peak antenna temperature ratios $^{12}\mathcal{R}(21)$ on the molecular cloud associated with rim G. The first two contours at 0.6 and 0.65 are thin-lined, dashed and solid, respectively. The following contours are at 0.7, 0.8, 0.9 and 1.0, and their weight increases with $^{12}\mathcal{R}(21)$. Positions where antenna temperature ratios have been deduced are indicated by circles. Bigger circles mark the positions which have been used for Fig. 19. Five spectra of a vertical strip (filled circles) with a typical behaviour concerning the line ratios are shown in Fig. 18. The UV flux of HD 206267 is responsible for the cloud's external heating (sketched by arrows). The positions of early-type B stars (up to B2) are also given. If the B2 star BD+57°2395B is as close as 1.5 pc, its UV flux incident on the cloud's surface is comparable to that of HD 206267.

diffuse gas, respectively. An even smaller and fainter globule (field 67), but also bright-rimmed, is located 7′ northeastward and shows a slightly higher negative velocity.

A further small cloud in the east (field 66) does not appear bright-rimmed, but line ratios $^{12}\mathcal{R}(21)$ of about 0.6 clearly indicate a warmer environment.

Like other weak features in our CO survey, fields 69 and 70 are interpreted as disappearing cloud remnants.

L1086: fields 71 to 75

L1086 has been observed only in ^{12}CO (1→0): Two clouds can be distinguished which are located on the border of IC 1396. L1086 E shows an interesting velocity structure which could be caused by the wind of nearby early-type B stars (cf. Fig. 9). Besides, an alignment of the peaks L1086 W and L1086 E with the faint emission around (−30,35) (fields 69 and 70) and the clouds associated with rims B and A on the sky (Fig. 4) and in the position-velocity map (Fig. 9) suggests an association of L1086 with IC 1396. We note that L1086 E coincides with a FIR maximum.

Only weak CO emission (fields 76 and 77) is found towards the extended FIR emission elongated in the southeast between the bright rims H and J, and B163 (field 184) is even regarded as not associated (see below).

Rim J: field 78

The rim J cloud is the smallest of the cloudlets in this survey. It is barely recognized. However, this small globule has been mapped with the IRAM 30 m telescope with a resolution of 20″ by Duvert et al. (1990) and found to be a highly fragmented, elongated filament with an internal bipolar outflow source. It is a remainder of the dissolving molecular cloud, but its appearance is evidence that even on the smallest size scales internal structure is encountered.

A small cloud (field 79) at +1.5 km/s is probably associated with IC 1396, because it is situated towards relatively strong extended FIR emission.

6.2. *Other clouds*

Here we briefly discuss all those clouds which lie in the line of sight towards IC 1396, but which are probably not associated with the H II region. Field numbers refer to Fig. 12 and Tables 3, 5, and 7.

Khav 161: fields 100 to 136

Our observations cover only the southeastern part of the broad curved dark lane Khav 161. Its outline is best traced in the ^{12}CO peak T_R^* map (Fig. 4) with B161 at the southeastern corner, Scho 1304 in the southwest and L1117 at (50,25), whereas the ^{13}CO map (Fig. 5) excellently contours four condensations on

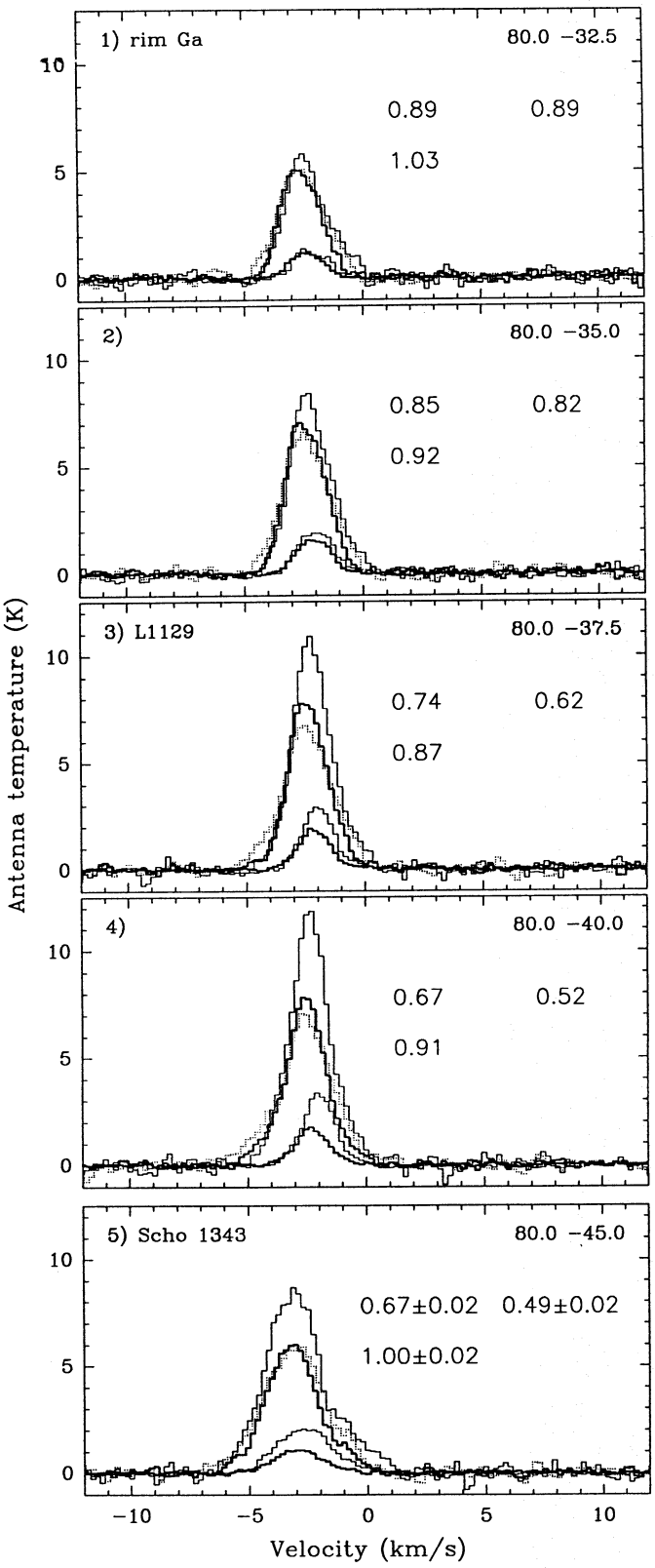

Fig. 18. Same as Fig. 13, but for positions along a vertical strip in the rim G cloud (cf. Fig. 17). Peak intensity ratios $^{12}\mathcal{R}(21)$, $^{13}\mathcal{R}(21)$ (upper values) and $^{12}\mathcal{R}(32)$ (lower value) are given. Going from NW (rim Ga) to SE (Scho 1343) the ratios do not change anymore significantly from offset (80, −40) on, and the ratios given in 5) are the mean ratios of the positions (80, −42.5), (80, −45) and (80, −47.5).

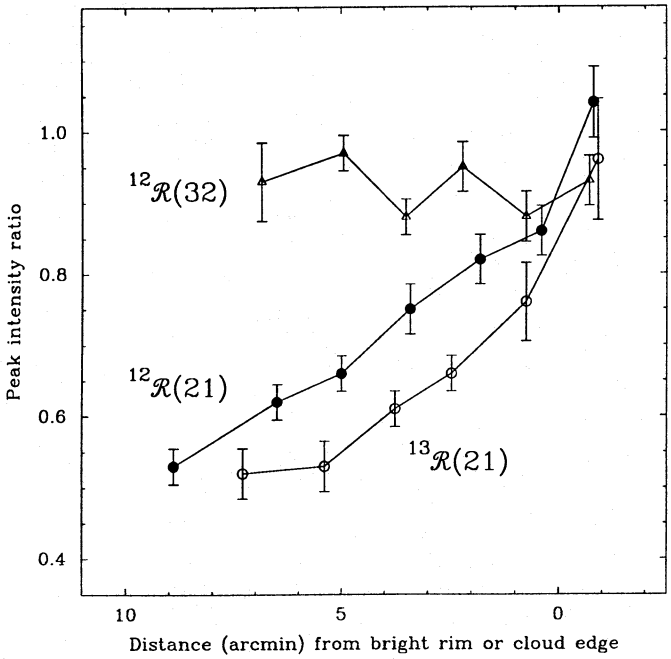

Fig. 19. Peak antenna temperature ratios in the dark clouds associated with rim G. The curves for $^{12}\mathcal{R}(21)$, $^{13}\mathcal{R}(21)$ and $^{12}\mathcal{R}(32)$ are based on 49, 36 and 34 measurements, respectively (cf. Fig. 17).

the border of or within Khav 161, i.e. B161, Anon DC, L1112, and L1128, and the central part of this lane, reaching from Scho 1314 to the northwest (see also Figs. 1 and 2).

Averaging the spectra in the southern part (fields 103 to 116), we find an almost gaussian line shape with widths of 1.9 and 1.35 km/s for ^{12}CO and ^{13}CO, respectively, at a velocity of −0.3 km/s. However, in the northern part (fields 122 to 131) the profiles are broader and not gaussian: For ^{12}CO we find a main and a secondary component at 0 and −1.5 km/s, respectively, the latter of which is somewhat more prominent in ^{13}CO.

The very dark globule B161 (fields 102 to 104) shows a comet-like appearance on the photograph with a head formed like the rim E cloud, but not bright-rimmed, and a tail turned away from HD 206267. It exhibits gaussian line shapes with broader widths in the tail at −0.55 km/s than in the head at −0.7 km/s: The line widths are 2.0 and 1.5 km/s for ^{12}CO and 1.0 and 0.9 km/s for ^{13}CO. In contrast to this appearance, we find no indication that B161 is associated with IC 1396, i.e. heated by HD 206267, e.g. from the backside: The peak T_R^* ratio $^{12}\mathcal{R}(21)$ is clearly less than 0.5 (a deeper probing $^{13}\mathcal{R}(21)$ is not available here). Leung et al. (1982) observed B161 with an angular resolution of 70″ using ^{12}CO and ^{13}CO lines and derived parameters for the globule assuming LTE.

Anon DC and L1112 are two dark markings located 20′ west and 18′ northwest of B161, respectively (see Fig. 2): The velocities are +0.55 and 0.0 km/s. In L1112 the ^{13}CO line is displaced by −0.35 km/s.

About 20′ further to the north is the dark patch L1117. We detected a ^{12}CO peak intensity of about 6.5 K at a velocity of −0.5 km/s, while almost no ^{13}CO was found, i.e. $\mathcal{R}(1) > 40$.

The globule and two adjoining short dark filaments, situated at the eastern border of Khav 161 and catalogued L1128, exhibit the narrowest lines observed in this survey: 1.15 and 0.6 km/s for ^{12}CO and ^{13}CO, respectively. Moreover, the ratio $\mathcal{R}(1)$ of 1.3 is the lowest in our data. The velocity is +1.1 km/s.

We name Khav 161 Core a more extended dark patch in the northwest of Scho 1314 at the border of the region observed in ^{13}CO. Two components were detected in ^{12}CO and ^{13}CO at −1.4 and +0.3 km/s, with the latter one more intense in ^{12}CO by a factor of about 2, while both ^{13}CO components have equal peak intensity (1.1 K).

Khav 156 (fields 137 to 139) lies adjacent to Khav 155 (and the B365 complex) in the sky, but the radial velocity is completely different, i.e. close to that of the most southern part of Khav 161.

B365 complex: fields 140 to 155

B365 is the elongated reversed S-like dark cloud in the southwest. The ^{13}CO peak T_R^* map (see Fig. 5) exhibits two cores at +8.0 km/s in the northwest (field 142/143) and in the southeast (141) and a weaker one at +7.65 km/s in the south (140). The average spectra (fields 140 to 152) are almost gaussian with line widths of 2.15 and 1.65 km/s for ^{12}CO and ^{13}CO, respectively.

Towards L1085 (fields 156 to 158) we observed three well-separated velocity components, at +2.8, +6.8, and −1.1 km/s, but only the former also shows distinct ^{13}CO emission, while the two latter are attributed to diffuse gas.

B160/L1083 complex: fields 161 to 181

The crab-shaped dark cloud B160 in the south is excellently traced in the ^{13}CO peak T_R^* map (Fig. 5) with the maximum where the photograph is darkest. The ^{12}CO lines observed around (−41,−67) seem to be self-absorbed. The line shapes in the average (fields 161 to 176) are non-gaussian for both ^{12}CO and ^{13}CO with a main component is at +8.0 km/s and a secondary at +6.4 km/s. Fitting two components, typical line widths are 2.25 and 1.6 km/s for ^{12}CO and ^{13}CO, compared to 2.8 and 2.1 km/s, respectively, for a fit with one gaussian.

A field close to the ^{12}CO T_R^* maximum has been observed in five lines (see Fig. 3), and Fig. 13 p shows the intensities of these spectra, typical for a cold dark cloud.

B160 is regarded as a cold foreground cloud, but the lines are as broad as or even broader than those of some bright rims, e.g. rims A and H, indicative of complex structure and high internal turbulence.

Concerning the distance towards the B160/B365 complex, we note that B157 and L1075 [at (l,b)=(96.7,+2.1)] also show velocities of +6.5 and +8.5 km/s, respectively (Robert & Pagani 1993), and that a distance of 400 pc towards B157 has been found from star counts (Tomita et al. 1979).

We note that field 183 shows rather high line ratios $^{12}\mathcal{R}(21)$ of about 0.7.

B163 and B163-SW: fields 184 and 185

The globule B163 shows a wind-swept appearance, but not directed in a sense that an association with HD 206267 might be suggested. The ^{12}CO line centre shows a velocity of +4.6 km/s. We found the line ratio $^{12}\mathcal{R}(21)$ to be less than 0.5. ^{12}CO and ^{13}CO emission at +4.8 km/s from B163-SW (9′ away) is as faint as that from B163. The globules were both the subject of several detailed studies (Martin & Barrett 1978, Arquilla & Goldsmith 1986).

B367 (field 186) shows very faint, but distinct emission in both ^{12}CO and ^{13}CO with a low $\mathcal{R}(1)$ of 1.5, and relatively small line widths (about 1.0 km/s).

The emission at +6 km/s towards field 187 and rim Db (Fig. 13 f) has already been mentioned by Heske & Wendker (1985).

7. Discussion

The molecular material associated with IC 1396 gives the appearance of being disrupted by the wind and radiation emanating from the exciting O6.5 star (HD 206267). Only a few clumps are left over from a former giant molecular cloud, which in earlier phases might have resembled e.g. the Orion GMC (Maddalena et al. 1986) and the Rosette Nebula (see e.g. Schneider et al. 1996).

A region very similar to IC 1396, the ring-like cloud system centered on the O8 star λ Ori, has been studied by Maddalena & Morris (1987), also in CO, H I and IRAS. Compared to the IC 1396 complex, the λ Ori clouds are more massive (by a factor of about 5), their velocities occupy a larger range, i.e. 15 km/s, and the diameter of the ring is larger as well, 70 pc.

A clumpy structure is a common property of molecular clouds (see e.g. Kwan & Sanders 1986, Tauber & Goldsmith 1990, Wilson & Walmsley 1989). Under the onslaught of the HD 206267 radiation, the bright-rimmed clouds seem to break up into many individual clumps, a process which has probably more advanced on rims H, C, and D, less on rim G, producing externally heated PDRs, which should offer an abundance of characteristic FIR and submm-lines, evidence of a high clump/interclump density contrast.

The mean velocity of the ionized gas of low surface brightness (emission measure of 1800 pc/cm^6, mean electron temperature of almost 6000 K) is about −2.0 km/s (Pedlar 1980). The values at 8 observed positions range from −4.5 to +0.6 km/s, which is close to the radial velocities of all bright rims (except rim A) (cf. Fig. 7). The radial velocity of the O6.5 star HD 206267 is about +6 km/s (cf. Wilson 1963), and its tangential velocity is 23 km/s directed to WSW, whereas the mean tangential velocity of 17 cluster members visually brighter than V=10.0 is 8 km/s directed to SW (cf. Marschall & van Altena 1987). Radial velocities of 4 B stars of Tr 37 (HD 205948, HDE 239712, HD 206183 and HDE 239729, for membership probabilities see Simonson 1968 and Marschall & van Altena 1987) are −5, −11, +10 and +8 km/s. The probable cluster member HD 206773 (Simonson 1968) (spectral type B0) has

a radial velocity of −8 km/s. Therefore the dispersion of the stellar velocities is larger than that of the rims, but the mean radial velocity of 0 km/s is very close to that of the rims and of the ionized material. We note that the radial velocities of the O8 star λ Ori and its associated cloud system also differ by about 10 km/s (Maddalena & Morris 1987).

The relative motion of clouds (mean radial velocity of −3 km/s) and HD 206267 (+6 km/s) along the line of sight is about 50 pc in 5 Myr. This is the size of a rather large giant molecular cloud, so that even if the clouds associated with rims were far from HD 206267 at the time of the formation of this star, it is likely that they were originally embedded in the same giant molecular cloud.

Wendker & Baars (1980) compared the average radial brightness temperature distribution of their radio continuum map to that expected on the basis of shell type models and proposed that the structure of IC 1396 is not due to matter moving radially outward, but is caused by a hot star approaching a few dense interstellar clouds. Moreover Heske & Wendker (1985), who observed about 40 positions in the IC 1396 region using the 6 cm H_2CO absorption line, suggested the B160/B365 complex in the south as the birthplace of HD 206267 because of their similar radial velocities.

Based on our data, we can propose a different three-dimensional model, assuming that a much larger cloud has been disrupted after the formation of Tr 37, which is now partly ionized, and that cloud fragments are now being driven radially outward. Material of the clouds associated with the rims A, B and G is found at higher negative velocities. The fact that rim B is brightest on the optical photograph (Fig. 1) might also be caused by the relative location of this and the other rims along the line of sight, compared to HD 206267. The rim A cloud then is located more on the front side of the H II region, thus nearest to the Sun. This agrees with our conclusion in Sect. 5.1 that rim A is located in front of the plane through HD 206267. Then, the higher radial velocity of rim A might be caused by interaction between the cloud and HD 206267.

8. Conclusions

The H II region IC 1396 is an outstanding object with respect to its global structure and geometry, i.e. distribution of molecular clouds in a shell-like structure, excitation essentially by only one central O6.5 star (HD 206267), and practically no confusion with fore- or background material along the line of sight.

Our CO multi-line survey and IRAS data reveal direct evidence for the interaction of radiation (and possibly stellar wind) with the molecular and dust clouds near HD 206267.

Using our ^{12}CO and ^{13}CO (1→0), H I and IRAS survey data and the optical photograph, we conclude:

- All bright-rimmed features A to J are prominent in CO (with the exception of the non-resolved rims C and J) as well as in the IRAS 12 to 100 μm maps, and the outlines already known from the optical photograph are traced nearly exactly. HD 206267 is situated near the northwestern border, i.e. inside, of a 1.5 deg^2 region which is free of molecular emission. It is also located at an equivalent position in a smaller "hole" of about 0.5 deg^2 in the IRAS maps. Furthermore, we detected in CO the more diffuse or dark clouds, without sharp edges, which are located near the centre and reaching to the north (Khav 161) and towards the south and southwest (B160/B365). These clouds are barely detected in the IRAS maps.
- Almost 20 bright-rimmed features are found in the radial velocity range between −8.3 and +1.7 km/s. The normal diffuse or dark clouds occupy two distinct velocity ranges, i.e. around 0 and +7 km/s.
- The projected radius of the bright-rimmed cloud system is 16 pc. We find no indications for a non-spherical geometry, i.e. linear distances which are considerably larger than the projected ones. In view of their brightness on the optical photograph and their radial velocities, only the clouds Ab, Ba, and Eb are thought to be behind, all others to be more or less in front of HD 206267.
- The total mass of the molecular clouds associated with IC 1396 (about 4000 $M_\odot$), the mass of the associated atomic gas (about 5000 $M_\odot$) and the mass of the H II (about 3000 $M_\odot$, cf. Matthews et al. 1980) are of the same order of magnitude. The molecular mass is small compared to that of other clouds near OB associations, and probably the bright-rimmed clouds are the last remnants of a once much larger giant molecular complex.
- Small and/or faint clouds which lie in projection and in velocity close to bright-rimmed objects are regarded as eroded fragments of these latter, now dissipating into the interstellar medium.
- H I observations of the IC 1396 region show several peaks which are associated with bright-rimmed clouds or the H II region, and HD 206267 is located on the southern border of a north−south-elongated "hole".
- Only close to the rims the peak T_R^* (1→0) values of the bright-rimmed clouds lie above those of the normal dark clouds.

Using our CO multi-line study of molecular clouds in the IC 1396 region, we can decide if a cloud is definitely associated with the H II region or not:

- Clouds associated with IC 1396 (mainly the bright-rimmed clouds, except rim E which shows strong self-absorption in ^{12}CO) exhibit the following excitation features:

(1) Near the bright rims the three transitions (1→0), (2→1) and (3→2) of ^{12}CO show within the errors the same peak T_R^*. The same is true for the ^{13}CO transitions.

(2) Elsewhere on bright-rimmed clouds the ^{12}CO (2→1) signal is less intense by a factor going down from almost 1.0 to 0.6 compared to the (1→0) spectrum, depending on the distance from the rim (or cloud edge). The same is true for ^{13}CO.

Everywhere on bright-rimmed clouds ^{12}CO (2→1) and (3→2) show the same peak T_R^* within experimental errors.

Such a molecular excitation scheme indicates the presence of a nearby strong heating source.

- Clouds not associated with IC 1396 (mainly Khav 161 and B160/B365) show significantly different excitation conditions:

(3) The ^{12}CO (2→1) peak T_R^* is at most half the ^{12}CO (1→0) value. The same is true for ^{13}CO.

Consistent with this behaviour, ^{12}CO (3→2) shows only about half the intensity of ^{12}CO (2→1).

This molecular excitation scheme is simple and in accord with that known for cold dark clouds without any interior or exterior heating source.

- High intertransitional line ratios towards bright-rimmed clouds indicate mean densities of about 4000/cm^3 and enhanced kinetic temperatures of more than 30 K in some of the stronger features and about 15 K in the less prominent clouds. Towards rim G we found a large gradient for T_{kin} in the plane of the sky.
- Strong self-absorption features in ^{12}CO spectra towards rim E and probably rim G are interpreted as caused by intrinsic temperature gradients.
- Atomic carbon emission in the form of the 492 GHz C I line was detected towards the rim A globule, suggesting that all bright-rimmed sources may be enshrouded in neutral and probably also in ionized atomic gas, as one expects from PDRs.

High spatial resolution measurements are required to understand more about the structure of all bright-rimmed clouds which is much smaller than the beam sizes used in our study.

Acknowledgements. H.W. gratefully acknowledges the financial support from the European Economic Community (contract number ST2-0305) and by the Deutsche Forschungsgemeinschaft (under contract We 1402/1−1). The authors thank the staff of the three observatories for their competent support.

All data reduction has been performed using the CLASS and GILDAS software developed at Groupe d'Astrophysique. This research has made use of the SIMBAD database operated at CDS, Strasbourg (France) and ESIS at ESA/ESRIN, Frascati (Italy).

The Nagoya 4 m radio telescope is operated by Nagoya University. The POM-2 2.5 m radio telescope on Plateau de Bure is operated by Observatoire de Grenoble on behalf of CNRS. The KOSMA 3 m radio telescope at Observatorium Gornergrat-Süd is operated by Universität zu Köln and supported by the Deutsche Forschungsgemeinschaft through grant SFB−301, as well as by special funding from the Land Nordrhein-Westfalen, and the observatory is administered by the Internationale Stiftung Hochalpine Forschungsstationen Jungfraujoch und Gornergrat, Bern (Switzerland).

IPAC is funded by NASA as part of the IRAS extended mission program under contract to JPL.

References

Abt H.A., 1986, ApJ 304, 688
Arquilla R., Goldsmith P.F., 1986, ApJ 303, 356
Avery L.W., White G.J., Williams I.P., Cronin N., 1987, ApJ 312, 848
Baars J.W.M., Wendker H.J., 1976, A&A 49, 473
Battinelli P., Capuzzo-Dolcetta R., 1991, MNRAS 249, 76
Barnard E.E., 1927, A Photographic Atlas of Selected Regions of the Milky Way, Part I: Photographs and Descriptions and Part II: Charts and Tables, Carnegie Institution, Washington
Becker W., Fenkart R., 1971, A&AS 4, 241
Beichman C.A., Neugebauer G., Habing H.J., Clegg P.E., Chester T.J., 1988, Infrared Astronomical Satellite (IRAS), Catalogs and Atlases, Volume 1, Explanatory Supplement, NASA, Washington
Bertoldi F., McKee C.F., 1992, ApJ 395, 140
Bhat C.L., Mayer C.J., Wolfendale A.W., 1986, Phil. Trans. R. Soc. London Ser. A 319, 249
Blomme R., 1990, A&A 229, 513
Brand J., Wouterloot J.G.A., 1994, A&AS 103, 503
Casoli F., Dupraz C., Gerin M., Combes F., Boulanger F., 1986, A&A 169, 281
Castets A., Lucas R., Lazareff B. et al., 1988, A&A 194, 340
Castets A., Duvert G., Dutrey A. et al., 1990, A&A 234, 469
Cernicharo J., 1985, ATM: A Program to Compute Theoretical Atmospheric Opacity for Frequencies <1000 GHz. Internal Report, IRAM, Grenoble
Clayton G.C., Fitzpatrick E.L., 1987, AJ 93, 157
Crampton D., Redman R.O., 1975, AJ 80, 454
Dibai E.A., 1969, Afz 5, 249
Dickman R.L., 1978, ApJS 37, 407
Dobashi, K., Bernard J.-P., Yonekura Y., Fukui Y., 1994, ApJS 95, 419
Duvert G., Cernicharo J., Bachiller R., Gómez-González J., 1990, A&A 233, 190
Fukui Y., 1989, Molecular Outflows: Their Implications on Protostellar Evolution. In: Reipurth B. (ed.), Low Mass Star Formation and Pre-Main Sequence Objects. ESO Proc. No. 33, ESO, Garching bei München, p. 95
Garibdzhanyan A.T., 1984, Astrophys. 20, 69
Garmany C.D., Stencel R.E., 1992, A&AS 94, 211
Georgelin Y.M., Georgelin Y.P., 1976, A&A 49, 57
Gierens K.M., Stutzki J., Winnewisser G., 1992, A&A 259, 271
Goldsmith P.F., Young J.S., Langer W.D., 1983, ApJS 51, 203
Guilloteau S., 1988, Spectral Line Calibration on the 30-m and 15-m Antennas. Internal Report, IRAM, Grenoble
Gyulbudaghian A.L., Rodríguez L.F., Curiel S., 1990, Rev. Mex. Astron. Astrofis. 20, 51
Gyulbudaghyan A.L., Rodriguez L.F., Canto J., 1986, Astrophys. 24, 119
Gyul'budagyan A.L., 1986, Astrophys. 23, 538
Hardorp J., Theile I., Voigt H.H., 1964, Luminous Stars in the Northern Milky Way, III. Internal Report, Hamburger Sternwarte and Warner and Swasey Observatory, Hamburg-Bergedorf
Herbig G.H., Rao N.K., 1972, ApJ 174, 401
Heske A., Wendker H.J., 1985, A&A 149, 199
Hildebrand R.H., 1983, QJRAS 24, 267
Humphreys R.M., 1978, ApJS 38, 309
Kalberla P.M.W., Mebold U., Reif K., 1982, A&A 106, 190
Kawabata K., Ogawa H., Fukui Y. et al., 1985, A&A 151, 1
Khavtassi J.Sh., 1960, Atlas of Galactic Dark Nebulae, Abastumani Astrophysical Observatory, Tbilisi
Klein R.I., Whitaker R.W., Sandford M.T., 1985, Processes and Problems in Secondary Star Formation. In: Black D.C., Matthews M.S. (eds.), Protostars & Planets II. The University of Arizona Press, Tucson, p. 340
Koyama K., Kawada M., Tawara Y. et al., 1991, ApJ 366, L19
Kun M., 1986, Ap&SS 125, 13
Kun M., Balázs L.G., Tóth I., 1987, Ap&SS 134, 211
Kun M., Pásztor L., 1990, Ap&SS 174, 13
Kutner M.L., Ulich B.L., 1981, ApJ 250, 341
Kwan J., Sanders D.B., 1986, ApJ 309, 783
Lada C.J., 1987, Star Formation: From OB Associations to Protostars. In: Peimbert M., Jugaku F. (eds.), Star Forming Regions. IAU Symp. 115, Reidel, Dordrecht, p. 1
Langer W.D., Goldsmith P.F., Carlson E.R., Wilson R.W., 1980, ApJ 235, L39
Laureijs R.J., Clark F.O., Prusti T., 1991, ApJ 372, 185
Leisawitz D., Bash F.N., Thaddeus P., 1989, ApJS 70, 731
Leung C.M., Kutner M.L., Mead K.N., 1982, ApJ 262, 583

Loren R.B., 1989, ApJ 338, 902
Loren R.B., Peters W.L., Vanden Bout P.A., 1975, ApJ 195, 75
Lynds B.T, 1962, ApJS 7, 1
MacLaren I., Richardson K.M., Wolfendale A.W., 1988, ApJ 333, 821
Maddalena R.J., Morris M., Moscowitz J., Thaddeus P., 1986, ApJ 303, 375
Maddalena R.J., Morris M., 1987, ApJ 323, 179
Marschall L.A., van Altena W.F., 1987, AJ 94, 71
Marschall L.A., Comins N.F., Karshner G.B., 1990, AJ 99, 1536
Martin R.N., Barrett A.H., 1978, ApJS 36, 1
Martin H.M., Sanders D.B., Hills R.E., 1984, MNRAS 208, 35
Matthews H.E., 1979, A&A 75, 345
Matthews H.E., Haslam C.G.T., Hills D.L., Salter C.J., 1980, A&A 88, 285
Nakano M., Tomita Y., Ohtani H., Ogura K., Sofue Y., 1989, PASJ 41, 1073
Parker N.D., 1988, MNRAS 235, 139
Patel N.A., Goldsmith P.F., Snell R.L., Hezel T., Xie T., 1995, ApJ 447, 721
Pedlar A., 1980, MNRAS 192, 179
Phillips T.G., Huggins P.J., Wannier P.G., Scoville N.Z., 1979, ApJ 231, 720
Plambeck R.L., Williams D.R.W., Goldsmith P.F., 1977, ApJ 213, L41
Pottasch S., 1956, Bull. Astron. Inst. Netherlands 13, 77
Robert C., Pagani L., 1993, A&A 271, 282
Röhrig R., 1990, Die Kalibration des KOSMA 3m Radioteleskops. Internal Report, I. Physikalisches Institut, Universität zu Köln, Köln
Schmidt E.G., 1974, MNRAS 169, 97
Schneider N., Stutzki J., Winnewisser G., 1996, A&A, submitted
Schoenberg, 1964, Veröffentl. Sternw. München 5, 313 (Nr. 21)
Schwartz P.R., 1985, ApJ 298, 292
Schwartz R.D., Gyulbudaghian A.L., Wilking B.A., 1991, ApJ 370, 263
Serabyn E., Güsten R., Mundy L., 1993, ApJ 404, 247
Sharpless S., 1959, ApJS 4, 257
Simonson S.C., 1968, ApJ 154, 923
Simonson S.C., van Someren Greve H.W., 1976, A&A 49, 343
Solomon P.M., Barrett J.W., 1991, The CO Luminosity – H_2 Mass Conversion Factor. In: Combes F., Casoli F. (eds.), Dynamics of Galaxies and Molecular Cloud Distribution. IAU Symp. 146, Kluwer, Dordrecht, p. 235
Stutzki J., Winnewisser G., 1985, A&A 144, 13
Sugitani K., Fukui Y., Mizuno A., Ohashi N., 1989, ApJ 342, L87
Sugitani K., Fukui Y., Ogura K., 1991, ApJS 77, 59
Sugitani K., Ogura K., 1994, ApJS 92, 163
Tauber J.A., Goldsmith P.F., 1990, ApJ 356, L63
Tomita Y., Saito T., Ohtani H., 1979, PASJ 31, 407
Trumpler R.J., 1930, Lick Obs. Bull. 14, 154
Walborn N.R., Panek R.J., 1984, ApJ 286, 718
Weikard H., Sugitani K., Duvert G., Miller M., 1991, An Extensive Study of Interstellar Matter in the IC 1396 Region using several Molecular Lines and Transitions of CO and Far-Infrared Maps from IRAS. In: Falgarone, E., Boulanger F., Duvert G. (eds.), Fragmentation of Molecular Clouds and Star Formation. IAU Symp. 147, Kluwer, Dordrecht, p. 513
Wendker H.J., Baars J.W.M., 1980, A&A 89, 180
White G.J., Phillips J.P., Richardson K.J., Harten R.H., 1986, A&A 159, 309
Whitworth A., 1979, MNRAS 186, 59
Wilking B.A., Blackwell J.H., Mundy L.G., 1990, AJ 100, 758
Wilson R.E., 1963, General Catalogue of Stellar Radial Velocities, Carnegie Institution, Washington
Wilson T.L., Walmsley C.M., 1989, A&AR 1, 141
Winnewisser G., Bester M., Ewald R. et al., 1986, A&A 167, 207
Winnewisser G., Zimmermann P., Hernichel J. et al., 1990, A&A 230, 248
Wootten A., Sargent A., Knapp G., Huggins P.J., 1983, ApJ 269, 147
Wouterloot J.G.A., Brand J., 1989, A&AS 80, 149
Wouterloot J.G.A., Brand J., Fiegle K., 1993, A&AS 98, 589
Wouterloot J.G.A., Fiegle K., Brand J., Winnewisser G., 1995, A&A 301, 236
Wouterloot J.G.A., Walmsley C.M., 1986, A&A 168, 237
Young J.S., Goldsmith P.F., Langer W.D., Wilson R.W, Carlson E.R., 1982, ApJ 261, 513

This article was processed by the author using Springer-Verlag LaTeX A&A style file version 3.